e-ISSN 2150-5551
CN 31-2103/TB

Nano-Micro Letters

ARTICLE

https://doi.org/10.1007/s40820-025-01813-1

Cite as
Nano-Micro Lett.
(2025) 17:315

Received: 1 April 2025
Accepted: 21 May 2025

Designing Metal Phosphide Solid-Electrolyte Interphase for Stable Lithium Metal Batteries Through Electrified Interface Optimization and Synergistic Conversion

Jung Been Park[1], Changhoon Choi[2], Min Sang Kim[1], Hyeongbeom Kang[1], Eunji Kwon[3], Seungho Yu[3,4], Dong-Wan Kim[1] ✉

HIGHLIGHTS

- Through strategic heterostructure design, it is possible to create electrified interfaces that induce the formation of a fully ionized depletion region and a built-in electric field.
- These electrified interfaces enhance Li affinity and promote uniform current distribution, leading to stable Li deposition behavior.
- Owing to intentional design, $SnP_{0.94}$/CoP heterostructure enables in situ conversion to a mixed ionic/electronic conductor during cycling, ensuring the long lifespan.

ABSTRACT Regulating the nucleation and growth of Li metal is crucial for achieving stable high-energy-density Li metal batteries (LMBs) without dendritic Li growth, severe volume expansion, and "dead Li" accumulation. Herein, we present a modulation layer composed of porous $SnP_{0.94}$/CoP *p-n* heterojunction particles (SCP), synthesized applying the Kirkendall effect. The unique heterointerfaces in the SCP induce a fully ionized depletion region and built-in electric field. This provides strong Li affinity, additional adsorption sites, and facilitated electron transfer, thereby guiding dendrite-free Li nucleation/growth with a low Li deposition overpotential. Moreover, the strategic design of the SCP, accounting for its reaction with Li, yields electronically conductive Co, lithiophilic Li–Sn alloy, and ionic conductive Li_3P during progressive cycles. The mixed electronic and ionic conductor (MEIC) ensure the long-term stability of the SCP modulation layer. With this layer, the SCP@Li symmetric cell maintains a low overpotential for 750 cycles even at a high current density of 5 mA cm^{-2}. Additionally, the $LiFePO_4$//SCP@Li full cell achieves an imperceptible capacity decay of 0.03% per cycle for 800 cycles at 0.5 C. This study provides insight into MEIC heterostructures for high-performance LMBs.

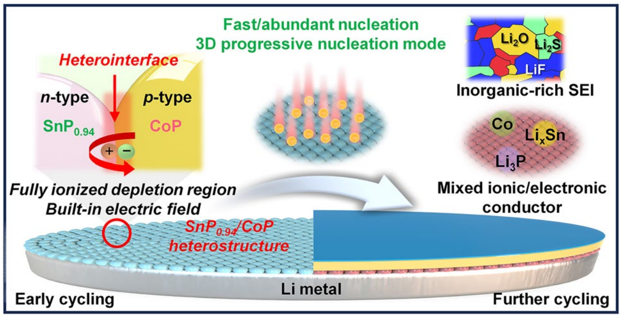

KEYWORDS Li metal batteries; Heterostructures; In situ reactions; Dendrite-free anodes; Mixed ionic/electronic conductors

---

Jung Been Park and Changhoon Choi have contributed equally to this work.

✉ Dong-Wan Kim, dwkim1@korea.ac.kr
[1] School of Civil, Environmental, and Architectural Engineering, Korea University, Seoul 02841, Republic of Korea
[2] Department of Materials Science and Engineering, SungShin Women's University, Seoul 01133, Republic of Korea
[3] Energy Storage Research Center, Korea Institute of Science and Technology, 5, Hwarang-ro 14-gil, Seongbuk-gu, Seoul 02792, Republic of Korea
[4] Division of Energy and Environment Technology, KIST School, Korea University of Science and Technology, Seoul 02792, Republic of Korea

Shanghai Jiao Tong University Press
Springer

1 Introduction

With the increase in global focus on environmental sustainability, secondary battery technology has advanced rapidly [1]. In addition, the growing demand for energy storage systems with higher energy densities (impelled by the rapid expansion of electric vehicles and consumer electronics markets) emphasizes the necessity of developing next-generation energy storage systems that surpass commercialized Li-ion batteries (LIBs) [2, 3]. Among the various candidates, lithium metal batteries (LMBs) constructed with Li metal anodes (LMAs) are widely considered as potential successors to LIBs for near-future energy markets because of their high theoretical capacity (3860 mAh g^{-1}), low redox potential (-3.04 V vs. standard hydrogen electrode (SHE)), and low gravimetric density (0.59 g cm^{-3}) [4, 5]. Nonetheless, the practical utilization of LMBs is impeded by persistent technical issues. The “hostless” LMAs with high reactivity can result in non-uniform Li-ion flux and irregular Li tip formation, which intensify the local charge density and electric field (called “tip effect”) [6]. Because the generated Li tips tend to evolve into Li dendrites, LMAs typically undergo infinite volume expansion and substantial mechanical stress, leading to damage the naturally formed solid electrolyte interphase (SEI) and the formation of inactive “dead” Li [7]. This mainly contributes to the continual consumption of organic electrolytes, degradation of electrochemical performance (particularly, the Coulombic efficiency (CE) and capacity decay), and safety hazard [8, 9]. Therefore, innovative approaches to stabilizing LMAs against dendrite formation and undesirable side reactions are essential for high-performance and safe LMB fabrication.

In response to the aforementioned challenges, numerous effective approaches have been proposed to mitigate the rambling growth of Li dendrites and side reactions, such as, adjusting the electrolyte composition [10, 11], introducing a modified separator [12], designing of 3D host/current collector [13, 14], adopting durable solid-state electrolytes [15, 16] and interfacial engineering of Li surfaces. Fine-tuning the electrolyte composition by adding functional additives (e.g., $LiNO_3$ [17], fluoroethylene carbonate [18], and heptafluorobutyrylimidazole [19]) can regulate the chemical composition and structure of the SEI. This ensures its relative stability in the short term. However, these additives are gradually consumed, resulting in the collapse of the SEI and its accumulation during the prolonged cycling of LMBs because of the high reactivity of Li [20]. Based on Sand’s time theory, 3D conductive host/current collectors with ample space, functioning as a “shelter” for LMAs, can effectively ensure reduced local current density and homogenized electric field/Li-ion flux distribution. Simultaneously, it can accommodate the volume expansion originating from the Li plating/stripping process [21, 22]. However, commonly studied 3D host and metal-based current collectors such as Cu and Ni foams tend to be excessively thick. These generally comprise over 83 wt% of the electrode [23]. Also, most require sophisticated synthesis techniques and pre-lithiation processes with limited Li storage capacity [24, 25]. Introducing solid-state electrolytes can improve the ion transportation efficiency, decrease the interfacial resistance, and increase the power output of LMBs [26, 27]. However, this approach typically entails a trade-off between mechanical strength and compatibility with LMAs [28]. The interfacial engineering directly on the LMA surface mainly involves (i) the construction of an artificial protective layer or SEI (inducing Li deposition below the artificial layer) and (ii) creating a modulation layer (inducing Li deposition above the modulation layer). This can effectively suppress dendrite growth and side reactions without compromising CEs during repeated Li plating/stripping processes. However, because of the insufficient electronic/ionic conductivity and mechanical stability of most reported protective layers and SEIs, these are typically effective only at relatively low current densities (< 3.0 mA cm^{-2}) [29]. In this regard, as a potential alternative strategy to enable long-term repeated Li plating/stripping at practical current densities higher than 3.0 mA cm^{-2}, the modulation layer on Li surfaces has recently attracted researchers’ attention. Preferably, to activate the anode electrolyte interface, the modulation layer should display a remarkable mixed electronic/ionic conductivity (MEIC) and high surface Li-ion affinity. First, owing to its high electronic/ionic conductivity, the modulation layer enables LMAs to enhance interfacial kinetics by reducing the concentration polarization at the interface through accelerated Li-ion dispersion and migration [30–32]. Second, the strong interfacial affinity for Li ions promotes uniform Li nucleation and increases the lateral diffusion of Li adatoms. This prevents the formation of 1D Li dendrites. Building on this synergistic effect, we

https://doi.org/10.1007/s40820-025-01813-1

can anticipate a preferable modulation layer to enable fast and uniform Li-ion flux distribution to provide adequate nucleation sites and induce lateral dendrite-free Li growth [33]. To realize these potential modulation layers, designing the chemical composition and microstructure of the materials is critically important.

Various lithiophilic inorganic materials have been proposed using diverse strategies for fabricating stable LMA. With respect to the most widely reported metal oxide/sulfides, although these lithiophilic species exhibiting strong interaction with Li ions can induce low nucleation overpotential and uniform Li nucleation/deposition of LMAs [34–36], inferior Li-ion conductive Li_2O/Li_2S is usually formed by a reaction between Li and the oxides/sulfides ($0 > \Delta G$). It is detrimental to the distribution of local ions/electrons and uniform Li plating/stripping [37]. Meanwhile, lithiophilic metal phosphides (e.g., Cu_3P [38, 39], Ni_3P [40], and CoP [41]) have recently been regarded as a noteworthy alternative class with relatively good electrical conductivity and chemical integrity. These can ensure a homogeneous Li-ion flux by using higher Li-ion conductive Li_3P (~10^{-4} S cm^{-1}, compared with Li_2O/Li_2S) synthesized from the reaction between Li and the phosphides [42, 43]. It is widely acknowledged that the interfaces of heterogeneous materials with elaborately designed microstructures can play a crucial role in controlling the interfacial charge redistribution and Li-ion adsorption capacity [44]. When two materials (A and B) are introduced into a heterojunction structure, electrons are transported spontaneously from material A with a higher Fermi level (E_F) to material B with a lower E_F until the E_F align. Depending on their band structures, these heterogeneous materials can form a fully ionized depletion region (FIDR). It provides abundant Li-ion adsorption sites and a built-in electric field (BIEF) that facilitates charge redistribution [45, 46]. Owing to the advantages of these heterointerfaces, previous studies reported the use of heterostructured materials for stable LMAs. However, many of these studies involved modifications to the 3D Li host or current collectors [47–49]. The modifications can cause the electrochemical or thermodynamic decomposition of the materials during the pre-lithiation process, thereby obscuring the advantages of the heterointerfaces. Furthermore, most reported materials are limited to oxide-based heterostructures (ZnO/CuO [28], TiO_2/Cu_2O [50], and MnO_2/ZnO [51]), whereas the low Li-ion conductivity of Li_2O formed during the pre-lithiation process is omitted.

Inspired by the above discussion, we successfully developed a novel tin phosphide ($SnP_{0.94}$)/cobalt phosphide (CoP) heterostructure (SCP) as the modulation layer for stable LMAs. The SCP was engineered meticulously to display a well-defined heterointerface, an extensive exposure of Sn/Co-P bonds, and a porous structure. This unique composition and heterostructure of the SCP have the following advantages: (1) The enhanced porosity of the SCP mitigates the local current density, while the increased exposure of Sn/Co-P relative to Sn/Co–O amplifies the advantageous heterointerface effect. (2) The heterointerface between CoP (*p*-type semiconductor) and $SnP_{0.94}$ (*n*-type semiconductor) forms a *p*-*n*-type heterojunction. This results in the generation of FIDR and BIEF. FIDR provides richer Li adsorption sites and higher Li adsorption energy. BIEF facilitates electron redistribution and Li-ion migration. (3) In terms of chemical composition, both CoP and $SnP_{0.94}$ have significantly higher Li binding energies than metallic Li. Thus, the synergistic effect between the lithiophilic $CoP/SnP_{0.94}$ and their heterostructure resulted in significantly enhanced Li deposition kinetics and a more uniform Li deposition behavior. Furthermore, during the repetitive Li plating/stripping process, lithiophilic Li_xSn, electronically conductive Co, and Li-ion conductive Li_3P formed by the spontaneous reaction between the SCP and metallic Li provided an MEIC layer. This ensured a stable Li deposition behavior during long-term cycling. With the aforementioned advantages, SCP@Li accomplishes dendrite-free Li deposition with an ultra-low nucleation overpotential (~2.2 mV) and the suppressed volume expansion even under a high areal capacity (5 mAh cm^{-2}). More remarkably, the symmetric cell with SCP@Li could be cycled stably 750 times even at a high current density of 5 mA cm^{-2}. The SCP@Li anode exhibited superior capacity and cycling stability in $LiFePO_4$ (LFP) and $LiNi_{0.8}Co_{0.1}Mn_{0.1}O_2$ (NCM811) full cells. The design strategy of heterostructured SCP as modulation layer on LMAs significantly contributes the enhancement of cell performance.

2 Experimental Section

2.1 Preparation of Heterostructured $SnP_{0.94}$/CoP (SCP)

First, $SnCo(OH)_6$, a precursor of SCP, was synthesized using a co-precipitation method. Two millimoles each of $Co(NO_3)_2·6H_2O$ (+98%, Sigma-Aldrich) and $C_6H_5Na_3O_7$ (99%, Alfa Aesar) were stirred in 70 mL of deionized water

(DW) for 30 min (solution A). Ten milliliters of 0.2 M $SnCl_4 \cdot 5H_2O$ (98%, Sigma-Aldrich) solution was added dropwise to solution A under vigorous stirring for 30 min (solution B). To adjust the pH to approximately 10, 10 mL of 2 M NaOH (98%. Samchun Chemicals) was added gradually to solution B using a burette. After vigorously stirring the solution for 1 h (color variation: purple → pink), the pink precipitates were obtained by centrifuging and rinsing with DW and ethanol solution, and dried at 70 °C for 24 h in a convection oven.

Second, the collected $SnCo(OH)_6$ products were mixed with NaH_2PO_2 using mortar and pestle for 5 min (molar ratio of $SnCo(OH)_6$:NaH_2PO_2 = 1:10) and heat-treated at 280 °C for 10 min at 10 °C min^{-1} with flowing Ar gas (20 sccm). After natural cooling, the black products were ground and washed using a 0.05 M HCl (36%, Samchun Chemicals) solution and DW. Finally, SCP was obtained after drying at 70 °C for 24 h in a convection oven.

2.2 Preparation of SCP Gas-phase Phosphidation

The $SnCo(OH)_6$ precursor and NaH_2PO_2 (molar ratio of $SnCo(OH)_6$:NaH_2PO_2 = 1:10) were placed at the center and in the upstream zone of a quartz tube, respectively, and heat-treated to 300 °C for 3 h with flowing Ar gas (20 sccm). The as-synthesized SCP gas-phase products were collected directly without additional washing.

2.3 Preparation of CoP

First, $Co(OH)_2$, a precursor of CoP, was synthesized via precipitation and hydrothermal methods. Ten millimoles of $Co(NO_3)_2 \cdot 6H_2O$ was dissolved in 20 mL DW. Then, 10 mL of 2 M NaOH solution was added (formation of precipitate). The solution was transferred to 60 mL Teflon-lined autoclave and heated for 2 h at 120 °C. The synthesized products were washed with DW and dried at 70 °C for 24 h in a convection oven.

Second, similar to the SCP synthesis, $Co(OH)_2$ was mixed with NaH_2PO_2 using a mortar and pestle for 5 min (molar ratio of $Co(OH)_2$:NaH_2PO_2 = 1:10) and heat-treated under conditions similar to those for SCP. After natural cooling, the black products were ground and washed using a 0.05 M HCl solution and DW. Finally, CoP was obtained after drying at 70 °C for 24 h in a convection oven.

2.4 Preparation of $SnP_{0.94}$

First, SnO_2, a precursor of $SnP_{0.94}$, was synthesized using precipitation and hydrothermal methods. Next, 10 mmol of $SnCl_4 \cdot 5H_2O$ was dissolved in 20 mL of DW, and 10 mL of 2 M NaOH solution was added (formation of precipitate). The solution was transferred to a 60 mL Teflon-lined autoclave and heated for 12 h at 160 °C. The synthesized products were washed with DW and dried at 70 °C for 24 h in a convection oven.

Second, similar to the SCP synthesis, SnO_2 was mixed with NaH_2PO_2 using a mortar and pestle for 5 min (molar ratio of SnO_2:NaH_2PO_2 = 1:100) and heat-treated under conditions similar to those for SCP. After natural cooling, the black products were ground and washed using a 0.05 M HCl solution and DW. Finally, $SnP_{0.94}$ was obtained after drying at 70 °C for 24 h in convection oven.

2.5 Materials Characterization

Field-emission scanning electron microscope (FESEM, Hitachi, SU-70) was used to analyze the morphology of $SnCo(OH)_6$, SCP, CoP, and $SnP_{0.94}$. The crystal structure was analyzed by X-ray diffraction (XRD, Rigaku, Miniflex 600 diffractometer) with Cu Kα radiation at a scanning rate of 2° min^{-1}. The Brunauer–Emmett–Teller (BET) surface areas and Barrett-Joyner-Halenda (BJH) pore size distributions were obtained using an N_2 adsorption–desorption process (MicrotracBEL Corporation, BELSORP-mas instrument) to compare the surface areas and pore distributions of $SnCo(OH)_6$ and SCP. The microstructure and elemental distribution of the SCP were observed using field-emission transmission electron microscope (FE-TEM, JEOL, JEM-F200) with energy-dispersive X-ray spectroscopy (EDS) detector. X-ray photoelectron spectroscopy (XPS, Thermofisher, Nexsa) with Al Kα radiation was applied to verify the chemical compositions and elemental valences. To determine the work functions of materials, UV photoelectron spectroscopy (UPS, Thermofisher, theta probe base system) measurements were performed with a helium discharge lamp ($h\nu = 21.2$ eV). The cross-sectional SEM and EDS images were captured after argon milling (accelerating voltage of 2 kV) using a cross-sectional ion polisher (JEOL, IB-19520CCP).

https://doi.org/10.1007/s40820-025-01813-1

2.6 Electrochemical Measurements

Firstly, the modified Li anodes with modulation layers were fabricated through drop casting method. The synthesized $SnP_{0.94}$, CoP, and SCP powders (10 mg) were stirred vigorously in 1 mL of toluene (99.8%, Sigma-Aldrich) for 3 h, and then 60 uL of the solution was dropped onto Li. After drying under vacuum at room temperature for 6 h, the modified Li anodes were obtained. All electrochemical characterization were conducted using CR2032-type coin cell, ether-based electrolyte (1 M lithium bis(trifluoromethanesulfonyl) imide (LiTFSI, 99.95%, Sigma-Aldrich) with 2 wt% $LiNO_3$ (99.99%, Sigma-Aldrich) in dioxolane (DOL, 99.8%, Sigma-Aldrich)/dimethoxyethane (DME, 99.5%, Sigma-Aldrich) at a volume ratio of 1:1), and a polypropylene separator (Celgard 2400). Galvanostatic and cyclic voltammetry (CV) tests were measured using an automatic battery cycler (WBCS 3000, WonATech Co.). Electrochemical impedance spectroscopy (EIS) profiles were recorded in the frequency range of 100 kHz to 0.01 Hz with an alternating voltage amplitude of 10 mV using IVIUMnSTAT electrochemical analyzer (IVIUM Technologies). For CE tests of asymmetric cells (Li//Cu), the charge cutoff voltage was set to 0.5 V *vs.* Li/Li^+. For full cell tests, $LiFePO_4$ (LFP, 1 C = 170 mAh g^{-1}) and $LiNi_{0.8}Co_{0.1}Mn_{0.1}$ (NCM811, 1 C = 200 mAh g^{-1}) as cathode materials was coated on an Al current collector with a homogeneously mixed slurry composed of LFP or NCM811:Super P carbon black (Alfa Aesar):polyvinylidene fluoride (PVDF, Kynar 2801) in a weight ratio of 8:1:1. The coated electrodes was dried at 70 °C for more than 8 h under vacuum. All full cells were activated for 1 cycle at 0.1 C. The mass loading of active materials (LFP and NCM811) was ~3.0 mg cm^{-2}. The galvanostatic charge/discharge tests of NCM811//Li full cells were measured in the potential window of 3.0–4.3 V (vs. Li/Li^+). For LFP//Li full cells, the potential window was set from 2.5 to 4.2 V (vs. Li/Li^+).

2.7 Measurement of Li^+ Diffusion Coefficient

To measure the Li^+ diffusion coefficient (D_{Li^+}), CV tests were conducted on the full cells at various scan rates (0.1, 0.2, 0.4, 0.6, 0.8, and 1.0 mV s^{-1}). D_{Li^+} was calculated by the Randles–Sevcik equation (Eq. 1) using the obtained CV curves that exhibited a linear relationship between the peak current (I_{peak}) and square root of the CV scan rate ($v^{0.5}$).

$$I_{\mathrm{peak}} = 2.69 \times 10^5 n^{1.5} \mathrm{A} \mathrm{D}_{\mathrm{Li}^+}^{0.5} \mathrm{C}_{\mathrm{Li}^+} v^{0.5} \tag{1}$$

where *n* is the number of electrons transferred, *A* is the surface area of the electrode, C_{Li^+} is the Li-ion concentration in the electrolyte, and v is the voltage scan rate.

2.8 Measurement of Ionic Conductivity

The ionic conductivity (σ) of the SCP modulation layer was measured by EIS using stainless steel (SS)|SCP coated glass fiber (GF/F, Whatman)|SS. The reason for using the SCP layer coated on GF via the vacuum filtration method was to measure the ionic conductivity of the SCP alone, without the influence of any binder. To compare the ionic conductivities of the SCP layers, SS|GF|SS was used as a blank cell. σ is calculated as follows Eq. 2.

$$\sigma = \frac{l}{R_{\mathrm{b}} S} \tag{2}$$

where l is the thickness of the separator, R_b is the bulk resistance, and S is the contact area of the SS.

2.9 Measurement of Activation Energy

To determine the activation energy of the SCP modulation layer, the ionic conductivity was measured at different temperatures. The activation energy (E_a) was calculated from a linear fit to the Arrhenius equation (Eq. 3):

$$\sigma = \sigma_0 \times e^{(-E_{\mathrm{a}}/RT)} \tag{3}$$

where R is the gas constant and T is the absolute temperature.

2.10 Finite Element Simulation

A finite element simulation was conducted using 3D modeling in COMSOL Multiphysics 6.3 to understand the electrodeposition process. Specifically, a tertiary current distribution module was used to investigate the current density (i_l) distribution on the LMA surface based on the Nernst equations (Eqs. 4 and 5):

$$J_{\mathrm{Li}} = -D_{\mathrm{Li}}\nabla c_{\mathrm{Li}} - z_{\mathrm{Li}}u_{\mathrm{Li}}Fc_{\mathrm{Li}}\nabla \emptyset_l \quad (4)$$

$$i_l = F\Sigma_{\mathrm{Li}}z_{\mathrm{Li}}J_{\mathrm{Li}} \quad (5)$$

where D_{Li} (0.5×10^{-9} m^2 s^{-1}), c_{Li} (1.0 M), z_{Li} (1.0), and u_{Li} represent the diffusion coefficient, concentration, charge number, and electric mobility of the Li ions, respectively. F and $\emptyset_l$ denote the Faraday constant (96,485 C mol^{-1}) and the electrolyte potential, respectively.

In the 3D modeling, the lithium metal anode was set to a size of 5×4.5 μm^2. Meanwhile, the diameters of the initial crystal nuclei were set to 0.55 and 0.15 μm for BLi and SCP@Li, respectively. The potential difference between the top and bottom (defined as the cathode and anode, respectively) was set to 0.02 V.

The electrochemical reaction for Li deposition on the electrode surface follows the Butler–Volmer equation (Eq. 6) shown below:

$$i_{\mathrm{Li}} = i_0\left[\exp\left(\frac{\alpha_{\mathrm{a}}F\eta}{\mathrm{RT}}\right) - \exp\left(-\frac{\alpha_{\mathrm{c}}F\eta}{\mathrm{RT}}\right)\right] \quad (6)$$

where i_0 is the exchange current density (i_0= 3 mA cm^{-2}), α_a is the anodic charge transfer coefficient (α_a= 1.5), α_c is the cathodic charge transfer coefficient (α_c= 0.5), and η is the overpotential.

2.11 Density Functional Theory (DFT) Computational Methods

First-principles calculations were carried out using the projector augmented wave method and the Perdew–Burke–Ernzerhof (PBE) generalized gradient approximation, as implemented in the Vienna Ab Initio Simulation Package (VASP). A plane wave basis set with a cutoff energy of 520 eV was employed for the calculations, and a gamma-centered $2 \times 2 \times 1$ grid was utilized for the k-point sampling. The electronic self-consistency and ionic relaxation loops were converged with criteria of 10^{-5} eV and 0.03 eV Å^{-1}, respectively. All calculations were spin-polarized, and van der Waals (vdW) interactions were accounted for using the DFT-D3 correction method. The calculations utilized the experimentally observed CoP(011) and $\mathrm{SnP_{0.94}}$(011) slabs. The adsorption energy of Li, $E_{\mathrm{ads\_Li}}$, was calculated using the formula $E_{\mathrm{ads\_Li}} = E_{\mathrm{all}} - E_{\mathrm{substrate}} - E_{\mathrm{Li}}$, where E_{all}, $E_{\mathrm{substrate}}$, and E_{Li} represent the total energies of all system, substrate, and Li atom, respectively. The charge density difference for the formation of the CoP(011)/$\mathrm{SnP_{0.94}}$(011) heterostructure, $\Delta\rho_{\mathrm{heterostructure}}$, was calculated using the formula $\Delta\rho_{\mathrm{heterostructure}} = \rho_{\mathrm{all}} - \rho_{\mathrm{CoP(011)}} - \rho_{\mathrm{SnP0.94(011)}}$, where ρ_{all}, $\rho_{\mathrm{CoP(011)}}$ and $\rho_{\mathrm{SnP0.94(011)}}$ represent the charge densities of all system, the CoP(011) component, and $\mathrm{SnP_{0.94}}$(011) component, respectively. Bader charge analysis was conducted using the Henkelman group's Bader charge analysis code to examine charge transport in the CoP(011)/$\mathrm{SnP_{0.94}}$ (011) heterostructure.

3 Results and Discussion

3.1 Fabrication of Heterostructured Tin Phosphide ($\mathrm{SnP_{0.94}}$) and Cobalt Phosphide (CoP)

The unique SCP with $\mathrm{SnP_{0.94}}$/CoP heterojunctions was fabricated using a two-step fabrication process. First, $\mathrm{SnCo(OH)_6}$ nanocubes, as precursors of SCP, were synthesized via a co-precipitation method (the procedures are detailed in the Experimental Section). After solid-state phosphidation (not gas-phase phosphidation with $\mathrm{PH_3}$) of $\mathrm{SnCo(OH)_6}$ at low temperature (280 °C) for a short time (10 min) by mixing with sodium hypophosphite, a heterostructured porous SCP was fabricated successfully with multitudinous advantages for LMAs. Figures 1a and S1a show a scanning electron microscope (SEM) image and X-ray diffraction (XRD) pattern of the $\mathrm{SnCo(OH)_6}$ intermediate products during the SCP fabrication process, respectively. The pink $\mathrm{SnCo(OH)_6}$ exhibited a well-defined nanocube morphology (average particle size = ~300 nm) and typical XRD pattern indexed to the perovskite hydroxide phase (PDF No. 26-1401). For the phosphidation of $\mathrm{SnCo(OH)_6}$, we introduced a solid-state phosphidation process (Eq. 7) [52] rather than the conventional gas-phase phosphidation process (Eqs. 8–11) [53] to simultaneously form a porous and clear heterogeneous phase of SCP.

$$\begin{aligned}&\mathrm{SnCo(OH)_6(s)} + x\mathrm{NaH_2PO_2(s)}\\&\quad\rightarrow \mathrm{SnP}_y\mathrm{(s)} + \mathrm{CoP}_z\mathrm{(s)} + x\mathrm{NaOH(s)} + \gamma\mathrm{H_2O(l)}\end{aligned} \quad (7)$$

$$\mathrm{3NaH_2PO_2(s) \rightarrow PH_3(g) + NaH_2PO_3(s) + Na_2HPO_3(s)} \quad (8)$$

$$\mathrm{4NaH_2PO_3(s) \rightarrow PH_3(g) + 2NaH_2PO_4(s) + Na_2HPO_4(s)} \quad (9)$$

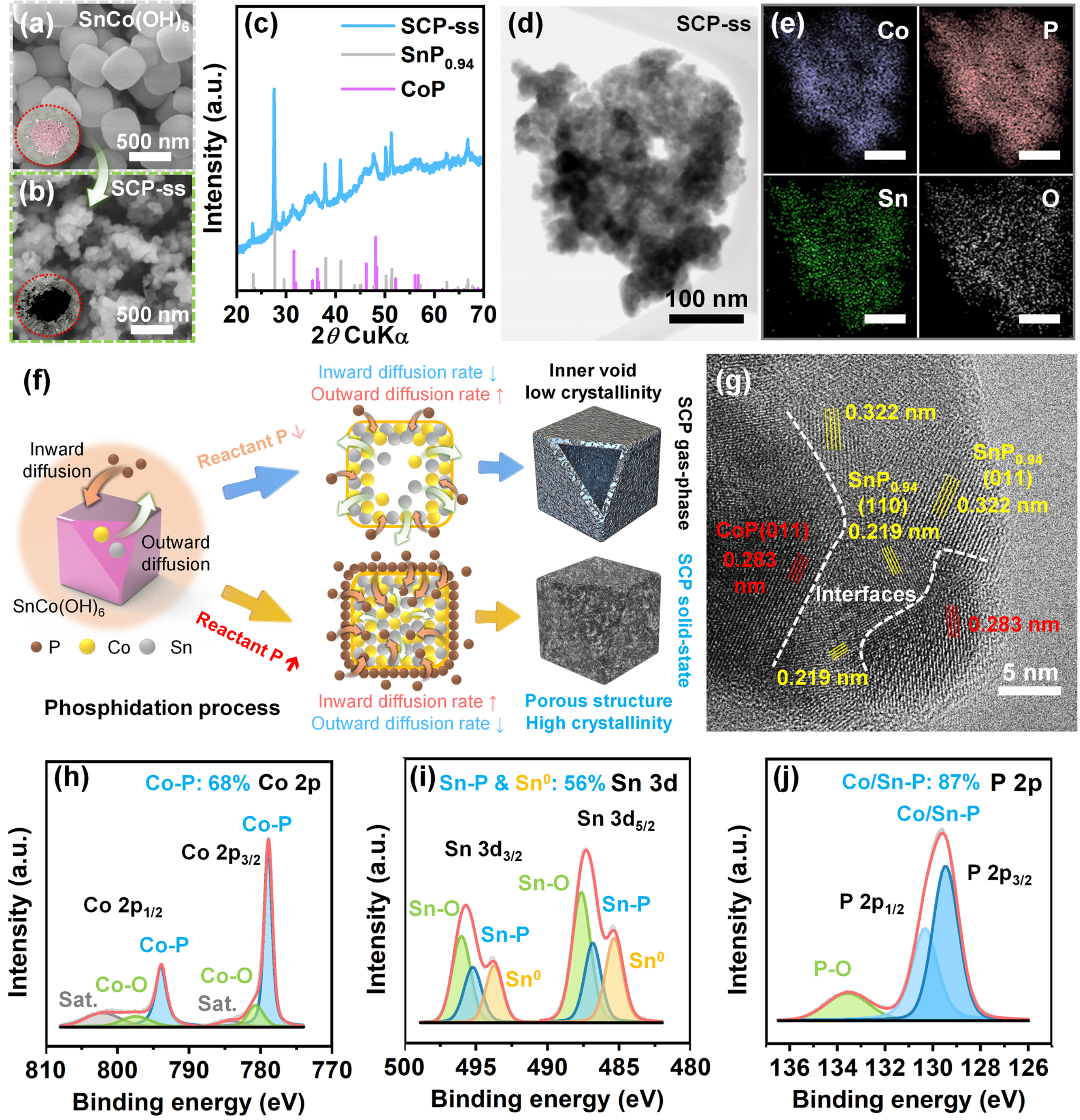

Fig. 1 Synthesis and characteristics of SCP. SEM images of **a** $SnCo(OH)_6$ and **b** SCP-ss (inset: digital images of $SnCo(OH)_6$ and SCP-ss powders). **c** XRD pattern of SCP-ss. **d** TEM image and **e** corresponding EDS elemental mapping images (scale bar: 100 nm) of SCP-ss. **f** Schematic illustration of the synthesis process of SCP according to the Kirkendall effect. **g** High-resolution TEM image of SCP-ss. XPS spectra of **h** Co 2*p*, **i** Sn 3*d*, and **j** P 2*p* of SCP-ss

$$4Na_2HPO_3(s) \rightarrow PH_3(g) + Na_2HPO_4(s) + 2Na_3PO_4(s) \quad (10)$$

$$SnCo(OH)_6(s) + xPH_3(g) \rightarrow SnP_y(s) + CoP_z(s) + \gamma H_2O(l) \quad (11)$$

For SCP synthesized via the gas-phase phosphidation process (denoted as SCP-gp), although the overall outer shape of $SnCo(OH)_6$ nanocubes was maintained, the nanoparticles contracted to a smaller size (~200 nm) with numerous nanosized bumps covering the surface of SCP-gp (Fig. S2a). The XRD pattern of SCP-gp reveals an amorphous structure without observable heterophase crystallinity (Fig. S2b). Notwithstanding the more intense thermal treatment conditions (300 °C and 3 h) of the gas-phase phosphidation process than those of the solid-state phosphidation process (280 °C and 10 min), the energy-dispersive X-ray spectroscopy (EDS) spectrum of SCP-gp exhibits a significantly low phosphorus-to-oxygen atomic ratio (P: 6.9 at%, O: 47.8 at%) (Fig. S3a). The amorphous structure and high oxygen content of SCP-gp imply a limited reactant P (sourced from PH_3 gas) concentration and low reactivity. Consequently, this does not satisfy the requirements for a distinct heterostructure and a high P/O ratio in the SCP. In contrast, the SEM image of the SCP synthesized via the solid-state phosphidation process (denoted as SCP-ss) displays a significantly reduced particle size (~150 nm) and porous structure (Figs. 1b and S4). Additionally, it exhibits a well-defined heterophase crystalline structure of $SnP_{0.94}$ (PDF No. 01-080-1201) and CoP (PDF No. 62-4588) compared with the amorphous SCP-gp (Fig. 1c). The enhanced porosity of SCP-ss was verified further by Brunauer–Emmett–Teller (BET) and Barrett-Joyner-Halenda (BJH) analyses (Fig. S5). SCP-ss demonstrates specific surface area (12.74 $m^2\ g^{-1}$) and pore volume (0.1033 $cm^3\ g^{-1}$) higher than those of $SnCo(OH)_6$ (7.64 $m^2\ g^{-1}$ and 0.0467 $cm^3\ g^{-1}$) and SCP-gp (5.21 $m^2\ g^{-1}$ and 0.0575 $cm^3\ g^{-1}$). This is favorable for inducing evenly Li-ion deposition and decreasing the local current density [4, 54]. Notably, in the inductively coupled plasma-optical emission spectrometer (ICP-OES) measurement and EDS spectrum (Figs. S6 and S3b), SCP-ss maintains the atomic ratio of Sn and Co at 1:1 but differs significantly from SCP-gp in that the proportion of P element (43.3 at%) is much higher than that of O element (14.1 at%). Therefore, the distinct heterophase crystalline structure, enhanced porosity, and abundant P content of SCP-ss make it a more potential candidate as a heterostructured material for facilitating stable Li behavior [42, 47]. To analyze the deeper microstructure and elemental distribution of SCP, transmission electron microscope (TEM) with EDS was used. As shown in Figs. 1d, e, and S7, SCP-ss was composed of a multitude of nanobubbles with a mean diameter of around 20 nm, and Co, Sn, P, and O were distributed uniformly without phase separation. The nanobubble structure observed after phosphidation originates from the nanoscale Kirkendall effect (Fig. 1f). During phosphidation process, Sn and Co ions typically exhibit an outward diffusion tendency to react with P to form SnP_x and CoP_x. Meanwhile, the diffusion of P ions is primarily inward, and driven by chemical potential and concentration gradients [55, 56]. As shown in Fig. S8, at low concentrations of reactant P (SCP-gp), the phosphidized product formed hollow inner voids owing to the diffusion rate of outward species (Sn and Co) being higher than that of the inward species (P). This is attributed to an insufficient concentration gradient of reactant P, which limits its rapid inward diffusion. Otherwise, at high concentrations of reactant P (SCP-ss), the significantly higher diffusion rate of the inward species than that of the outward species resulted in the formation of porous structures combined with numerous nanopores and nanobubbles within SCP-ss via the Kirkendall effect in localized areas (Figs. 1d and S7). Furthermore, the high-resolution TEM image of SCP (Fig. 1g) shows distinct interfaces between the lattice fringes of the $SnP_{0.94}$ ((110) and (011) crystal planes, corresponding to interplanar distances of 0.219 and 0.322 nm, respectively) and lattice fringe CoP ((011) crystal plane, corresponding to an interplanar distance of 0.283 nm), indicating the presence of $SnP_{0.94}$/CoP heterointerface. The fast Fourier transform (FFT) pattern (Fig. S9) also demonstrates distinguishable lattices corresponding to the $SnP_{0.94}$(011), CoP(011), $SnP_{0.94}$(110), and CoP(211) planes, from the innermost to the outermost rings, respectively.

X-ray photoelectron spectroscopy (XPS) was used to analyze the elemental composition and valence states of SCP-ss. The Co 2*p* spectrum (Fig. 1h) exhibited three distinct spin-orbital split peaks (Co $2p_{1/2}$ and Co $2p_{3/2}$). The dominant component is at 793.8 and 778.9 eV corresponding to the Co-P bond in the Co^{3+} oxidation state [57, 58]. It accounts for 68% of the spectral area. Two additional sets of peaks at 798.5/780.6 eV and 803.3/784.2 eV correspond to the Co–O bond (Co^{2+}) and satellite peaks, respectively [59, 60], accounting for ~17% and ~15% of the spectral area. The Sn 3*d* spectrum (Fig. 1i) also shows three sets of doublet peaks (Sn $3d_{3/2}$ and Sn $3d_{5/2}$) at 495.6/487.2 eV, 494.8/486.4 eV, and 493.3/484.9 eV, corresponding to Sn–O (Sn^{4+}), Sn-P (Sn^{2+}), and Sn metal (Sn^0), respectively [61, 62]. The presence of the Sn^0 peak is attributed to the metallic β-Sn-like bonding in the $SnP_{0.94}$ crystal structure [63, 64]. Thus, similar to the Co 2*p* spectrum, the

https://doi.org/10.1007/s40820-025-01813-1

fraction of valence states associated with $SnP_{0.94}$ (Sn^{2+} and Sn^0) is ~56%. It is more abundant than the Sn-O bonds. The P 2*p* spectrum (Fig. 1j) is deconvoluted into three peaks at 133.5, 130.3, and 129.4 eV, corresponding to P-O, Co/Sn-P (P $2p_{1/2}$), and Co/Sn-P (P $2p_{3/2}$) bonds, respectively [42, 58]. Although superficial oxidation results in the formation of P-O (~13% in the P 2*p* spectral area), Co-O, and Sn-O bonds, the degree of superficial oxidation in the SCP-ss is significantly lower than that in SCP-gp (Fig. S10) and previously reported transition metal phosphides synthesized via the gas-phase phosphidation process [42, 45, 65]. This indicates a higher density of exposed Sn/Co–P bonds and their interfaces in SCP-ss. Based on a comparative study between SCP-ss and SCP-gp, we designated SCP-ss simply as SCP hereafter.

3.2 Understanding the Band Structure and Its Impact in SCP

The distinctive characteristics of heterostructures are not realized only through the formation of heterojunctions between different materials. Typically, the unique merits of heterostructures are closely linked to specific microstructures with distinct band structures of the heterointerfaces. Therefore, we analyzed the band structures of $SnP_{0.94}$ and CoP to evaluate whether SCP can provide favorable heterointerfaces. $SnP_{0.94}$ and CoP were prepared through a solid-state phosphidation process analogous to that for SCP (Fig. S11). To thoroughly investigate the band structure of $SnP_{0.94}$ and CoP, the work function (ϕ_{Wf}), valence band maximum (E_{VBM}), and band gap (E_g) energies of each material were obtained by ultraviolet photoelectron spectroscopy (UPS) spectra, XPS valence band spectra, and UV–visible absorption spectra, respectively (Fig. S12). The energy positions of ϕ_{Wf}, E_{VBM}, and E_g for $SnP_{0.94}$ and CoP are summarized in Table S1. Based on the calculated energy levels of $SnP_{0.94}$ and CoP, the energy diagrams before and after the contact between $SnP_{0.94}$ and CoP are illustrated in Fig. 2a. The band diagram shows that $SnP_{0.94}$ is an *n*-type semiconductor with E_F higher than that of CoP. Meanwhile, CoP is a *p*-type semiconductor with E_F lower than that of $SnP_{0.94}$. Therefore, after $SnP_{0.94}$ and CoP come into contact, the energy bands at the heterointerfaces spontaneously align until the E_F of the two materials attains equilibrium, as the electrons (the majority carriers of the *n*-type semiconductor) of $SnP_{0.94}$ and the holes (the majority carriers of *p*-type semiconductor) of CoP recombine at the heterointerfaces [66]. As a result, the partially intrinsic electroneutral region near the heterointerfaces is ionized by formatting the FIDR and generate to charge separation. This, in turn, yields region of localized positive and negative charge [67]. These charged regions function as active sites for electrochemical reactions and effectively adsorb oppositely charged species. In addition, the charge separation region in the FIDR leads to BIEF, thereby facilitating charge redistribution by the additional electric field force. This effectively distributes the charge density and alleviates the intense local current density. The charge redistribution and beneficial effects at the SCP heterointerfaces were further confirmed by density functional theory (DFT) calculations. We set $SnP_{0.94}(011)$ and CoP(011) as representative crystal planes based on the exposed crystal planes observed in the TEM image of the SCP (Fig. 1g). The differential charge density simulation (Fig. 2b) at $SnP_{0.94}$/CoP heterointerface demonstrated that a net electron of 2.54*e* according to the Bader analysis transfers from $SnP_{0.94}$ to CoP [68]. This is consistent with the calculated band structure model (Fig. 2a). Therein, the n-type semiconductor $SnP_{0.94}$ (displaying E_F higher than that of CoP) functions an electron donor. The interactions between Li atoms and the $SnP_{0.94}$, CoP, and $SnP_{0.94}$/CoP heterointerface were also calculated to evaluate their lithiophilicity. The adsorption sites of Li atoms (E_{ads}) on $SnP_{0.94}$, CoP, and $SnP_{0.94}$/CoP heterointerface were selected after an initial screening of adsorption trends on the surface (Fig. 2c). As shown in Fig. 2d, E_{ads} of $SnP_{0.94}$ ($SnP_{0.94}$-H: −2.41 eV), CoP (CoP-T/H: −2.22/−2.98 eV), and $SnP_{0.94}$/CoP heterointerface ($SnP_{0.94}$/CoP-1/2/3: −3.14/−3.12/−3.23 eV) are significantly higher than the Li cohesive energy (−1.41 eV), indicating that $SnP_{0.94}$, CoP, and their heterointerface can provide favorable nucleation sites to lower Li nucleation barrier. Interestingly, among them, the highest E_{ads} of $SnP_{0.94}$/CoP heterointerface suggests that the well-designed heterointerface can supply more Li adsorption sites and enhance the Li nucleation kinetics more than $SnP_{0.94}$ or CoP [49]. Profiting from the abundant Li adsorption sites and superior Li nucleation kinetics of $SnP_{0.94}$/CoP heterointerface based on DFT calculation, we evaluated the nucleation overpotential (NOP) of the Li anodes applied with SCP as modulation layer (SCP@Li) at a current density of 0.5 mA cm^{-2} (Fig. 2e). SCP@Li exhibits an exceptionally reduced NOP (~2.2 mV) compared with those of bare Li (BLi, ~44 mV), $SnP_{0.94}$@Li (~16.2 mV), and CoP@Li (~4 mV). It has a

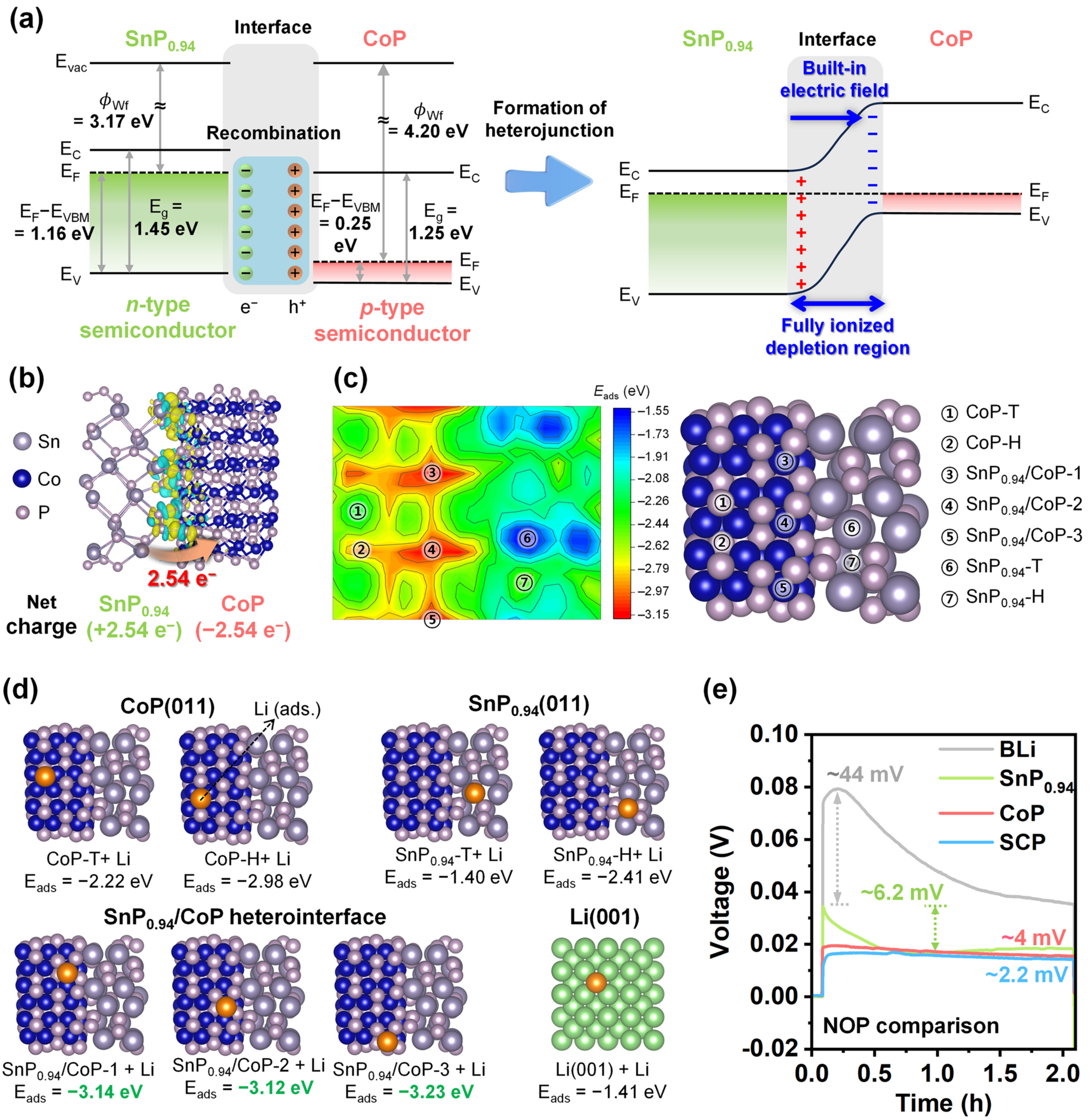

Fig. 2 Band structure and its impact evaluation for SCP. **a** Schematic diagram of energy levels before and after contact between $SnP_{0.94}$ and CoP. **b** Differential charge density of $SnP_{0.94}$/CoP heterointerface (yellow area: electron accumulation, cyan area: electron depletion). **c** Contour plot of adsorption energy of Li on $SnP_{0.94}$/CoP heterostructure. **d** E_{ads} on Li(001), CoP(011), $SnP_{0.94}$(011), and CoP(011)/$SnP_{0.94}$(011) heterointerface. **e** Voltage–time profiles of BLi, $SnP_{0.94}$@Li, CoP@Li, and SCP@Li at a current density of 0.5 mA cm^{-2}

trend similar to that of the DFT calculations of E_{ads}. This implies that $SnP_{0.94}$, CoP and SCP can all effectively lower the Li nucleation barrier more than BLi, but SCP with heterointerface can further promote the phase transition of Li ions on the SCP surface. Furthermore, as shown in Fig. S13, at the Li growth step corresponding to the steady-state voltage, the lowest overpotential of SCP@Li also indicates that the SCP markedly helps reduce the voltage polarization and improve the Li deposition kinetics during the Li deposition process.

3.3 Revealing the Li Deposition Mechanism on SCP@Li

To scrutinize how the SCP modulation layer affects the initial nucleation and further growth of Li, the Li deposition behavior as a function of the stepwise deposition capacity was analyzed by ex-situ SEM. Surface and cross-sectional SEM images of the pristine SCP@Li show that the SCP layer is formed with a thickness of ~ 11 µm without cracks on the Li foil through optimized coating conditions (Fig. S14). When Li of 0.05 mAh cm^{-2} were deposited on BLi and SCP@Li at a current density of 1 mA cm^{-2}, the initial Li nucleation behaviors of BLi and SCP@Li showed significant differences (Fig. S15). The huge hexagonal initial Li nuclei (~4.7 µm) on BLi (Fig. S15a) can be attributed to the preferential growth of metallic Li (body-centered cubic (bcc) crystal structure) along the [111] direction, which minimizes the surface energy by maximizing the exposure of the {110} planes [69]. In contrast, in SCP@Li (Fig. S15b), metallic Li is deposited uniformly on the SCP surface composed of countless SCP nanoparticles (~150 nm), forming small Li nuclei and smooth surface without generating prominent micro-sized Li nuclei. As shown in Figs. 3a, b, and S16, the difference between the initial nucleation steps of BLi and SCP@Li had a significant impact on the subsequent Li growth behavior. After Li deposition of 0.1 mAh cm^{-1}, BLi gradually formed dendritic and porous Li deposits in three steps (I: Li nucleation; II: heterogeneous growth around the nuclei; and III: entanglement through continuous growth). The patchy and dendritic Li growth on BLi is mainly attributed to the limited number of Li nucleation sites and low surface Li diffusivity, which favorably deposited Li ions locally at the initial nucleation sites with an increased local current density [5]. This malicious Li deposition behavior of BLi persists up to 5 mAh cm^{-2}. The highly porous Li deposits affect the increase in voltage polarization and decrease in cell lifetime because the pores devour a considerable amount of electrolyte (causing electrolyte dry-out and violent side reactions) and accelerate the volume expansion of the LMA during repetitive Li plating/stripping [70]. For SCP@Li, with the altered Li nucleation behavior, lateral Li growth dominates after Li deposition of 0.1 mAh cm^{-2}, and is sustained up to 5 mAh cm^{-2}. This leads to the formation of dense and dendrite-free Li deposits. In addition, as shown in Fig. S16, the grain size of SCP@Li is observably smaller than that of BLi after Li deposition of 5 mAh cm^{-2}, suggesting that the initially small and abundant Li nuclei in SCP@Li significantly influenced the subsequent deposition behavior [2]. The stable Li deposition behavior of SCP@Li is further confirmed even at high current densities (3 and 5 mA cm^{-2}). As shown in Fig. S17, BLi still shows non-uniform and island-like Li deposits at low magnification. At high magnification, the surface of Li deposits is composed of clusters of moss-like nanodendrites, unlike under a low current density of 1 mA cm^{-2}. The change in Li deposition behavior of BLi under high current densities is evidence for the low surface Li diffusivity and lacking nucleation sites of BLi. This deficiency accelerates the growth of small needle-like dendritic structures and the non-uniformity of Li deposits as the current density increases. In stark contrast, SCP@Li still maintains the dense and dendrite-free Li deposition behavior even under high current densities. The difference in Li deposition kinetics between BLi and SCP@Li becomes more pronounced in the galvanostatic profiles recorded at high current density during Li deposition (Fig. S18). Thus, the stable Li deposition behavior of SCP@Li demonstrates that the SCP modulation layer can provide abundant lithiophilic Li nucleation sites and enhance Li diffusivity. This, in turn, yields a uniform Li-ion/electric field distribution during the Li deposition process. To further investigate the effect of the SCP modulation layer on the Li deposition behavior, cross-sectional backscattered electrons (BSE) and EDS elemental mapping images of BLi and SCP@Li after Li deposition of 5 mAh cm^{-2} were analyzed. The contrast variation in the BSE images (directly related to the difference in atomic number) allows for the distinction between the metallic Li and SEI components. As shown in Fig. 3c, the Li deposits on BLi exhibited a loosely packed chunk morphology and protrusions with a thickness of ~102.9 µm. Also, combined BSE and EDS elemental mapping analyses revealed that the surface of the porous Li deposits was predominantly covered by SEI components, which were formed by the reactions between the electrolyte and metallic Li. The observed results provide compelling evidence of the challenges (electrolyte dry-out, accumulation of SEI components, and volume expansion) associated with the porous Li deposition behavior on BLi. In sharp contrast, the compact Li deposits without protrusions on SCP@Li (thickness: ~35.4 µm) (Fig. 3d) showed an effective suppression of volume expansion during high-capacity Li deposition while maintaining the SCP modulation layer stably (Fig. S19). It is noteworthy that compared with the

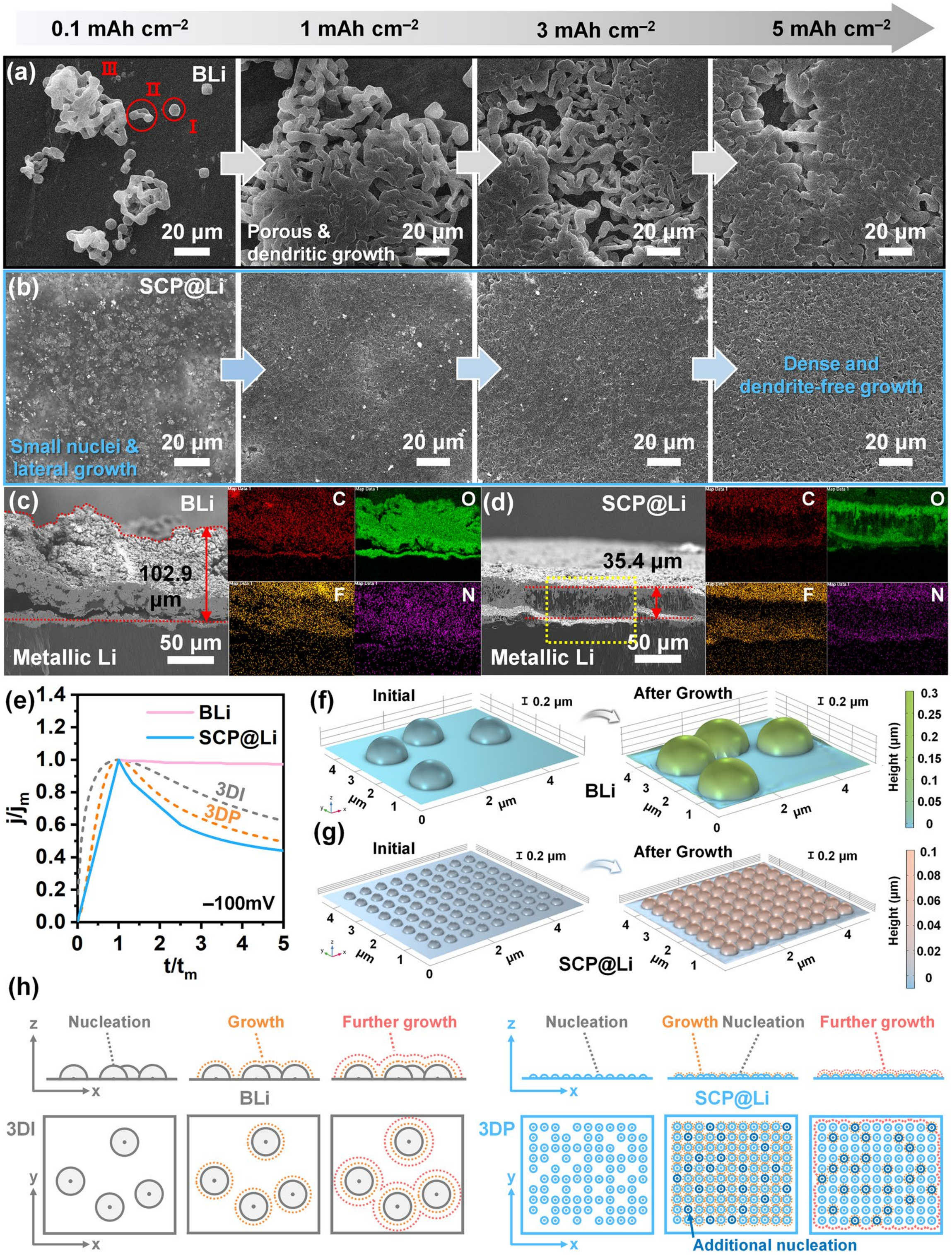

Fig. 3 Li deposition behavior of SCP@Li. Ex-situ SEM images of **a** BLi and **b** SCP@Li after Li deposition at a fixed current density of 1 mA cm^{-2} with areal capacities of 0.1, 1, 3, and 5 mAh cm^{-2}. Cross-sectional BSE and EDS images of **c** BLi and **d** SCP@Li after Li deposition of 5 mAh cm^{-2}. **e** Dimensionless plot of experimental current transients of Li metal deposition using BLi and SCP@Li. Simulated initial nuclei models and final Li deposition models of **f** BLi and **g** SCP@Li after 100 s of Li deposition. **h** Schematic illustration of the Li nucleation and growth mechanism of BLi and SCP@Li

https://doi.org/10.1007/s40820-025-01813-1

deposited BLi, significantly few components were obtained from the SEI within the dense Li deposition layer on SCP@Li. This indicates that the Li deposition behavior of SCP@Li can also mitigate the side reactions between the electrolyte and Li deposits. The stable Li deposition behavior of SCP@Li was also verified by constant-current polarization tests using symmetric cells at a current density of 5 mA cm^{-2}. In the test, glass fibers (GF/F, Whatman) were used as a separator to analyze the rapid and clear short circuits inside the cell system. As shown in Fig. S20, an abrupt voltage reduction in the symmetric BLi cell (indicating an internal short circuit) was recorded at ~0.24 h. In contrast, SCP@Li sustained Li deposition without observable internal short circuit for ~1.69 h, which was approximately seven times longer than that of the BLi cell. These results strongly support the capability of SCP@Li to guide stable Li deposition even at a high current density.

Given that the electrocrystallization of new phases is closely related to overpotentials, we employed chronoamperometry (CA) technique to record the potentiostatic current transients (Fig. S21). Subsequently, the current transients were normalized to dimensionless transients using the peak current (j_m) and its corresponding time (t_m) as reference points to gain a deeper insight into the Li nucleation mechanism. A comparison of the dimensionless transients with the Scharifker–Hills model for 3D instantaneous (3DI) and progressive (3DP) nucleation allows for the determination of whether the initial nuclei are generated instantaneously at the beginning or through a progressive process over time. The mathematical equations of the model are as follows (Eqs. 12 and 13) [71]:

$$\text{3DI:}\quad \left(\frac{j}{j_m}\right)^2 = 1.9542\left(\frac{t}{t_m}\right)^{-1}\left\{1-\exp\left[-1.2564\left(\frac{t}{t_m}\right)\right]\right\}^2 \tag{12}$$

$$\text{3DP:}\quad \left(\frac{j}{j_m}\right)^2 = 1.2254\left(\frac{t}{t_m}\right)^{-1}\left\{1-\exp\left[-2.3367\left(\frac{t}{t_m}\right)^2\right]\right\}^2 \tag{13}$$

As shown in Fig. 3e, although both BLi and SCP@Li are difficult to detect because of their rapid electrochemical reactions at the initial stage prior to t_m [72, 73], BLi and SCP@Li are closer to the 3DI and 3DP nucleation models after t_m, respectively. The 3DI nucleation of BLi was characterized by the depletion of a limited number of nucleation sites during the very early nucleation. In addition, because the ideal 3DI model does not consider reactions other than Li deposition, the large deviation between the ideal 3DI model and the dimensionless transient curve of BLi originates from the continuous electrolyte decomposition reaction. This suggests an excessive electrolyte consumption and an unstable SEI of BLi during Li nucleation and growth [73]. By contrast, SCP@Li displayed a j_m (10.57 mA cm^{-2}) substantially higher than that of BLi (0.29 mA cm^{-2}), attributing to the numerous active sites and high nucleation rate according to Scharifker's theory (Fig. S21) [71, 74]. And the 3DP model, similar to the Li nucleation behavior of SCP@Li, indicates the progressive activation of nucleation sites accompanied by concurrent nuclei growth. This typically give rise to the formation of smaller particles [75]. The different nucleation modes of BLi and SCP@Li influence the local electrochemical environment, thereby affecting the subsequent growth patterns. Finite element simulations were performed utilizing COMSOL Multiphysics to delve deeper into the post nucleation step. The size and number of the initial Li nuclei on BLi and SCP@Li were determined based on the SEM results. As depicted in Fig. S22, in the initial step (0 s), the current density vectors were focused on the limited nuclei on BLi, whereas those in SCP@Li displayed a high degree of uniform spatial distribution throughout a large number of progressively generated nuclei, yielding a more uniform Li-ion flux. In the Li growth process (Fig. S23), the preferential deposition of Li ions onto pre-existing nuclei exacerbated the non-uniform and localized Li growth behavior in BLi, ultimately leading to the formation of detrimental protrusions (Fig. 3f). However, owing to the homogeneous distribution of the current density and Li-ion flux, the Li nuclei on SCP@Li underwent uniform and planar growth, suppressing excessive volume expansion and protrusions (Fig. 3g).

Based on the aforementioned experimental and simulation results, a Li nucleation and growth mechanism for BLi and SCP@Li is proposed (Fig. 3h). For BLi, the limited number of Li nucleation sites, high Li nucleation barrier, and 3DI nucleation mode yield non-uniform and large Li nuclei within a significantly short timeframe during the initial nucleation process. Subsequently, Li ions are concentrated on these random Li nuclei without additional Li nucleation during the Li growth process. This further intensifies the localized Li deposition and eventually causes severe volume expansion and Li protrusions. Unlike BLi, because the SCP modulation layer has abundant Li nucleation sites, a low Li nucleation barrier, and a 3DP nucleation mode, minute and numerous Li nuclei are generated progressively and uniformly over the initial nucleation process. The effectively modulated Li nuclei ultimately grow into a close-packed Li deposition layer capable of suppressing dendritic growth, volume expansion, and side reactions between the electrolyte and Li deposits. The modulated Li deposition behavior of SCP@Li is the foundation for improving the electrochemical kinetics and reversibility of LMBs.

3.4 Assessing the Electrochemical Characteristics of SCP@Li

To investigate the influence of the SCP modulation layer on electrochemical kinetics, various electrochemical characterizations of symmetric and asymmetric cells with BLi and SCP@Li electrodes were performed. Figure 4a shows the typical centrosymmetric loops of cyclic voltammetry (CV) profiles of the BLi and SCP@Li symmetric cells [76]. Furthermore, compared with BLi (0.30 mA cm^{-2}), the CV profiles of SCP@Li demonstrate larger current responses (8.41 mA cm^{-2}) in the 1st cycle and a higher coincidence in the selected (the 1st, 5th, and 10th) cycles (Fig. S24). This demonstrates the better reversibility of Li plating/stripping and improved interfacial electrochemical reaction kinetics [77]. To investigate the electrochemical reactions during Li plating/stripping of SCP, symmetric CV tests were additionally performed over wider potential windows (Fig. S25). Based on the results of CV tests, the SCP undergoes gradual transformation primarily through a spontaneous reaction with Li metal, leading to the formation of Li-Sn alloy capable of reversible electrochemical reaction. In particular, although the SCP modulation layer can result in gradual modification of the SEI composition during repeated Li plating/stripping, the well-overlapped CV curves of SCP@Li symmetric cell indicate that the formed SEI displays a remarkable excellent electrochemical stability [78]. A similar tendency is observed in the CV curves of the asymmetric Li//Cu cells at a sweep rate of 2 mV s^{-1} (Fig. S26). Typically, the two redox peaks at approximately 0 V in the CV curves indicate Li plating/stripping on the working electrodes [79]. The cell with SCP@Li displays higher peak current densities (stripping peak current density ($J_{\text{peak,strip}}$): 7.86 mA cm^{-2}, plating peak current density ($\text{J}_{\text{peak,plate}}$): 6.79 mA cm^{-2}), and a lower onset potential of lithiation (100 mV, inset of Fig. S26) compared with BLi ($\text{J}_{\text{peak,strip}}$: 1.70 mA cm^{-2}, $\text{J}_{\text{peak,plate}}$: 1.21 mA cm^{-2}, onset potential: 130 mV). This clearly indicates the enhanced electrochemical redox kinetics realized by SCP@Li. The exchange current density (j_0) was measured to compare the reaction kinetics at the electrode/electrolyte interface. If the effects of concentration polarization are insignificant at the interface, j_0 can be calculated from the Tafel equation according to the CV curves (Fig. 4b) [21]. The j_0 of the SCP@Li symmetric cell (1.67 mA cm^{-2}) is higher than that of the BLi symmetric cell (0.063 mA cm^{-2}). This result implies improved charge transfer capability and faster interfacial electrochemical reactivity in the SCP@Li symmetric cell, which is in agreement with the CV results of the symmetric cells [21]. The Li-ion conduction and desolvation was measured via temperature-dependent electrochemical impedance spectroscopy (EIS) using cells with blocking electrodes and Li symmetric cells (Figs. S27 and S28). Prior to the evaluation of Li-ion conduction and desolvation resistance, the ionic conductivity (σ) of the cell with the SCP layer (calculated from the EIS spectra at room temperature) exhibited 10.0 mS cm^{-1}. This was almost 1.77-fold higher than that of the blank cell (5.65 mS cm^{-1}). Also, by linear fitting of the Arrhenius equation, the activation energies (E_a) of SCP layer were determined as 2.74 and 39.54 kJ mol^{-1} for Li-ion conduction and desolvation, respectively (Figs. S27c and 4c). The high σ and low E_a of the SCP modulation layer verifies the important roles of SCP in accelerating the Li-ion desolvation effect and Li-ion transportation owing to higher Li-ion adsorption energy and BIEF of SCP heterostructure and, thereby, mitigating the adverse effects of increased electrode thickness [80–82].

To validate the long-term durability and reversibility of SCP@Li for LMBs, the galvanostatic cycling performance of the SCP@Li symmetric cells was measured and compared with those of other symmetric cells with BLi, CoP@Li, and $\text{SnP}_{0.94}$@Li electrodes. As shown in the voltage–time profiles at a current density of 1 mA cm^{-2} with the plating capacity fixed at 1 mAh cm^{-2} (Fig. 4d), SCP@Li exhibited the lowest overpotential with remarkable cycling stability for ~1200 h. The remarkably reduced overpotential can be indexed to the various advantages of the lithiophilic CoP/$\text{SnP}_{0.94}$ heterostructure (including the uniform redistribution of Li ions and charge at the heterointerface, stable SEI formation, and dense Li deposition without dendrites) [47]. Conversely, the BLi and CoP@Li symmetric cells suffered a gradual increased polarization and voltage oscillation after ~525 and ~725 h, respectively. This is attributed to the rapid increase in impedance resulting from the severe

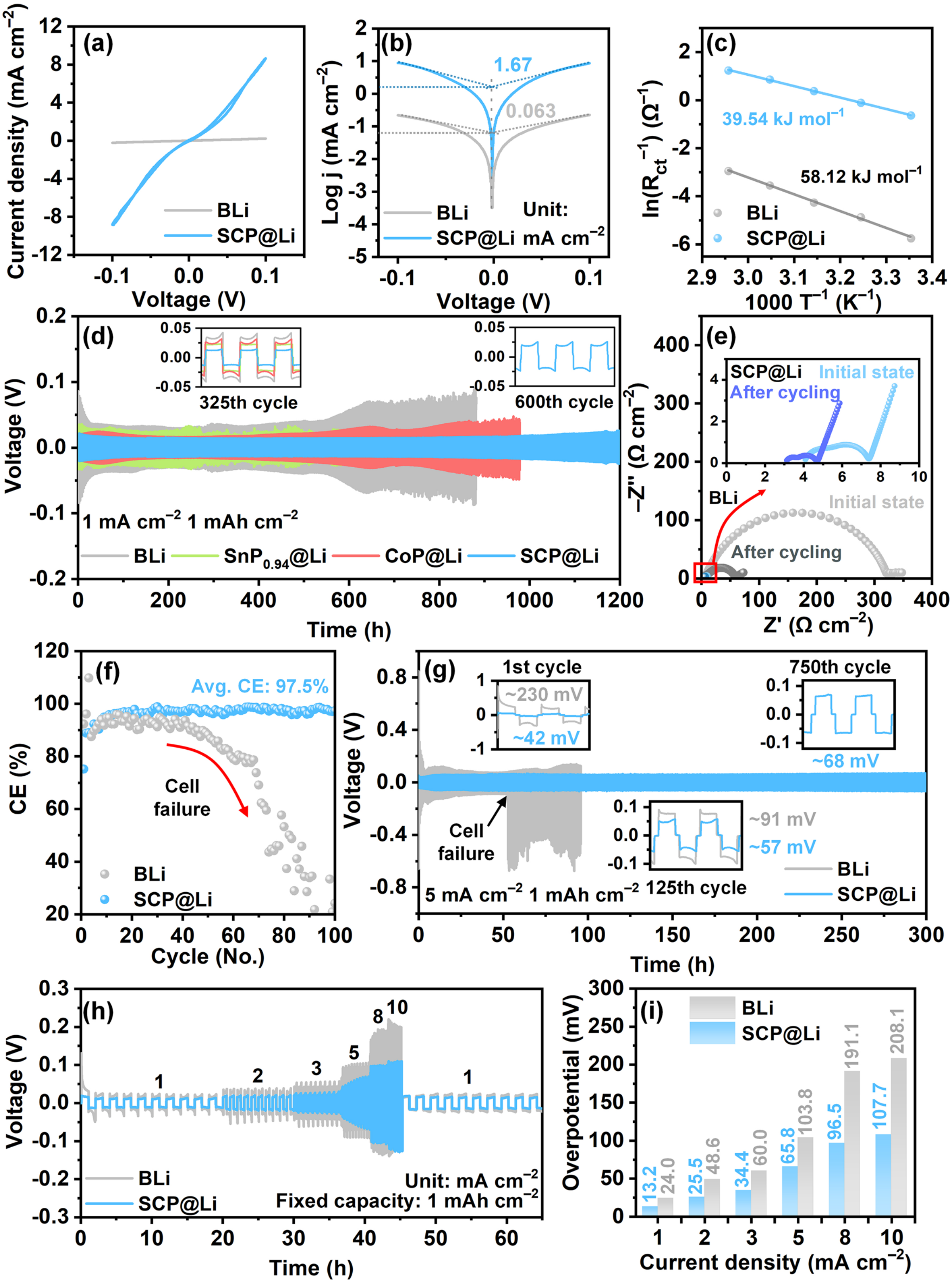

Fig. 4 Electrochemical analysis of SCP@Li. **a** CV curves and corresponding **b** Tafel plots of BLi and SCP@Li symmetric cells. **c** Activation energies for Li^+ desolvation. **d** Voltage–time profiles under a current density of 1 mA cm^{-2} with a plating capacity fixed at 1 mAh cm^{-2}. **e** Nyquist plots at initial state and after 10 cycles of BLi and SCP@Li symmetric cells. **f** CEs of Li deposition on BLi and SCP@Li asymmetric cells. **g** Voltage–time profiles under a current density of 5 mA cm^{-2} with a plating capacity of 1 mAh cm^{-2}. **h** Rate performance of BLi and SCP@Li symmetric cells. **i** Comparison of overpotentials of BLi and SCP@Li symmetric cells corresponding to Fig. 4h

side reactions including electrolyte consumption and accumulation of inactive "dead Li" during repeated Li plating/stripping [50]. Unlike the others, the voltage–time profile of $SnP_{0.94}$@Li (Fig. S29) exhibited intense fluctuations followed by a dramatic voltage decrease after ~ 600 h, indicating conventional soft short circuit in Li symmetric cells [83, 84]. As seen in the insets of Fig. 4d, SCP@Li exhibited a marginal overpotential (14.5 mV, 325th cycle). Meanwhile, BLi, CoP@Li, and $SnP_{0.94}$@Li exhibit 41.3 mV, 31.6 mV, and 23.1 mV, respectively. Additionally, the SCP@Li symmetric cell exhibits a gradual polarization over 1200 h without an illusion of long-term cycle performance originating from the hard short-circuit in the cell. This indicates an ultra-slow controlled consumption of active Li and minimal "dead Li" formation during the prolonged cycling [21, 85]. To further investigate the electrochemical reaction kinetics of the assembled symmetric cells, the Nyquist plots of the BLi and SCP@Li symmetric cells was obtained before/after cycling at 1 mA cm^{-2} with 1 mAh cm^{-2} (Fig. 4e and Table S2). By fitting electrochemical resistance values based on the equivalent circuit (Fig. S30), the interfacial resistance (R_{int} = the resistance of SEI (R_{SEI}) + the charge transfer resistance (R_{ct})) of the BLi symmetric cell fell from ~307.4 to ~53.7 Ω after 10 cycles, indicating the increased surface area due to porous Li deposits generated during Li plating/stripping [5]. With regard to the SCP@Li symmetric cell, the initial R_{int} value (~3.0 Ω) was much smaller than that of the BLi cell, ascribed to elevated electrochemical kinetics and active surface area by introducing the SCP modulation layer [86]. After 10 cycles, the R_{int} value of SCP@Li decreased to ~ 1.54 Ω. This further confirmed the gradual SEI stabilization and the formation of the smooth deposited Li surface without Li dendrites during the initial plating/stripping process. Furthermore, the decreased R_{bulk} and R_{int} are attributed to the gradual formation of Li_3P and inorganic-rich SEI (further discussed in the section on SCP transformation after cycling), which is composed of highly Li-ion conductive species [87]. Specifically, at an equal current density, the SCP@Li renders a higher average CE (~97.53%) for 100 cycles. This suggests the high reversibility of Li plating/stripping behavior on the SCP modulation layer. Meanwhile, BLi exhibits remarkable CE drops after 40 cycles (Fig. 4f). We also evaluated the cycling stability of the symmetric cells in a harsher current density of 5 mA cm^{-2} with fixed capacity of 1 mA cm^{-2}. As shown in Fig. 4g, the SCP@Li symmetric cell maintained a low overpotential (~68 mV) for up to 300 h (= 750th cycle) with a significantly flat voltage plateau. However, the voltage–time profiles of the BLi symmetric cell exhibited intense voltage fluctuations throughout the cycles, which intensified after 53 h (= 132th cycle) owing to uncontrollable Li dendrite growth. The superior cycling performance of SCP@Li was compared with previously reported surface-modified LMAs, as summarized in Table S3. To validate the reversibility of the symmetric cells under variable current densities, we conducted rate tests on the BLi and SCP@Li symmetric cells at a fixed capacity of 1 mAh cm^{-2} (Fig. 4h). The sequential implementation of current densities of 1, 2, 3, 5, 8, and 10 mA cm^{-2} yielded stair-shaped voltage–time profiles. This is indicative of corresponding stepwise increased overpotentials. The cells using SCP@Li/BLi presented overpotentials of 13.2/24.0, 25.5/48.6, 34.4/60.0, 65.8/103.8, 96.5/191.1, and 107.7/208.1 mV, respectively (Fig. 4i). Here, SCP@Li demonstrated a significantly lower overpotential at each stage and an approximately two-fold lower overpotential than BLi at the maximal current density of 10 mA cm^{-2}. The key reason for the remarkable rate performance of the SCP@Li symmetric cell is likely to be the combination of a high rate of diffusion during Li-ion dissolution and the rapid Li-ion conductivity at the electrolyte/SCP@Li interface [28]. In contrast, the BLi symmetric cell sustained irreversible critical damage under increased current densities (≥ 8 mA cm^{-2}). This was inferred from the observation of rapidly increasing overpotentials. Moreover, when the current density decreased to 1 mA cm^{-2}, the overpotential (~15.8 mV) in the SCP@Li symmetric cell returned to be similar values, indicating unobstructed Li-ion transfer pathways within the electrode and its outstanding cycling reversibility and durability.

3.5 Monitoring the Chemical Transformation of SCP and Morphological Evolution in SCP@Li after Cycling

To reveal the effect of SCP modulation layer, the morphological evolution of BLi and SCP@Li was investigated after 50 cycles (100 h) at a current density of 1 mA cm^{-2} under an areal capacity of 1 mAh cm^{-2}. The high (Fig. 5a) and low (Fig. S31a) magnification SEM images of the Li-deposited BLi surface show loosely connected, non-uniform deposits with inconsistent sizes, as well as significantly accumulated lumps of pulverized "dead Li" and broken SEI layers. The Li-stripped BLi surface (Figs. 5b and S32a) further revealed deleterious lumps, in conjunction SEI shells originating from the dissolution of reversible Li deposits. The surface morphology of the cycled BLi demonstrates the non-uniform, porous Li deposition behavior and the resulting irreversibility of BLi. This irreversibility deteriorates the lifetime and electrochemical kinetics of LMBs during subsequent cycling owing to the rapid electrolyte and fresh Li consumption and an increased resistive fraction [88]. In contrast, the Li-deposited SCP@Li (Figs. 5c and S31b) still displays compact and dendrite-free Li deposition layer consisting of relatively homogeneous "cell-like" Li deposits over a broad area. In particular, as shown in Figs. 5d and S32b, the key distinction between Li-stripped SCP@Li and BLi is that SCP@Li exhibits only SEI shells with a morphology identical to that of Li deposits observed on the Li-deposited SCP@Li without inactive Li accumulation and destroyed SEI. This indicates a reversible Li plating/stripping within the SEI shells analogous to the breathing process of the lungs [89]. These observations also emphasize the important role of the SCP modulation layer in enhancing reversibility and eliminating malicious inactive components.

Beyond optimizing Li deposition, the variation in the chemical composition of the SCP modulation layer and the SEI component evolution of SCP@Li after cycling were investigated. Before cycling, the XRD patterns (Fig. S33) and XPS spectra (Fig. S34a–c) of SCP@Li verified the retention of the pristine SCP powders. To further understand the spontaneous reaction between SCP and Li metal, XPS depth profiling analysis was performed on pristine SCP@Li and a thinner SCP layer-coated Li. As shown in Fig. S34d, even after sufficient Ar^+ sputtering for 30 min, pristine SCP@Li exhibited no significant difference from the P 2*p* XPS spectrum before depth profiling, without any trace of Li_3P, the conversion product of CoP and $SnP_{0.94}$. For SCP in close contact with Li (thin coating layer), a small fraction of Li_3P was observed along with transition metal phosphide bonding (Fig. S34e). The existence of Li compound between SCP layer and Li metal is also evidenced in Li 1*s* spectrum (Fig. S34f). This XPS depth profiling analysis indicates that although some conversion reaction occurred in the lower layer in contact with Li before cycling, the original SCP composition was well maintained throughout the SCP layer. After 50 cycles at a current density of 1 mA cm^{-2} under a capacity of 1 mAh cm^{-2}, the disappearance of the SCP crystalline phase and the observation of only metallic Li peaks in the XRD pattern of SCP@Li indicate the transformation of SCP into an amorphous phase (Fig. S33). XPS depth profiling analysis was employed to examine the transformation of the SCP during cycling (Fig. 5e). Prolonged sputtering revealed distinct peaks corresponding to the constituent elements of the SCP. After 5 min of Ar^+ sputtering, the cycled SCP@Li showed a significant reduction in the intensity of the peaks associated with the pristine SCP (Fig. 1h–j). Concurrently, new peaks corresponding to Co^0 (791.5/775.87 eV) [90], Li_xSn (490.3/481.9 eV) [91], and Li_3P (127.2/126.3 eV) [92] became dominant in the Co 2*p*, Sn 3*d*, and P 2*p* XPS spectra. The conversion of CoP and $SnP_{0.94}$ to metallic Co, Li_xSn alloy, and Li_3P is attributed to the strong reducing potential of metallic Li, which ultimately resulted in compositional variations within the SCP [41]. Because the SCP modulation layer was designed to maintain its function as an MEIC that can simultaneously transport Li ions and electrons, unlike electron-insulating layers or purely electron-conductive layers, even with compositional variations during cycling, SCP@Li can stably induce Li plating/stripping processes over extended cycles by synergistically incorporating metallic Co (high electronic conductivity), Li-Sn alloy (high Li affinity) [93], and Li_3P (high ionic conductivity). The introduction of an SCP modulation layer can also influence the SEI by regulating its composition during long-term cycling and adapting the environment to promote efficient Li plating/stripping [94]. Thus, the SEI components of SCP@Li and BLi after cycling were evaluated further via XPS depth profiling (Figs. 5f and S35). In terms of C 1*s* XPS spectra, before Ar^+ sputtering, both cycled BLi and SCP@Li mainly revealed organic components including C–O (286.5 eV, originated from DOL/DME solvent decomposition or remnants), C=O and O–C=O (288.1 and 289.7 eV, respectively, originated from the decomposition products of the solvents), and $–CF_3$ (292.8 eV, originated from the decomposition or remnants of $TFSI^-$ anion) [95]. However, with an increase in Ar^+ sputtering time, the intensity of the organic species reduced gradually within the cycled BLi and SCP@Li. Meanwhile, SCP@Li exhibited a significantly lower proportion of organic species (particularly C=O and O–C=O) than BLi (Fig. S36). Moreover, the newly appearing C-Li peak (282.5 eV) of SCP@Li indicates the likely presence of metallic Li after Ar^+

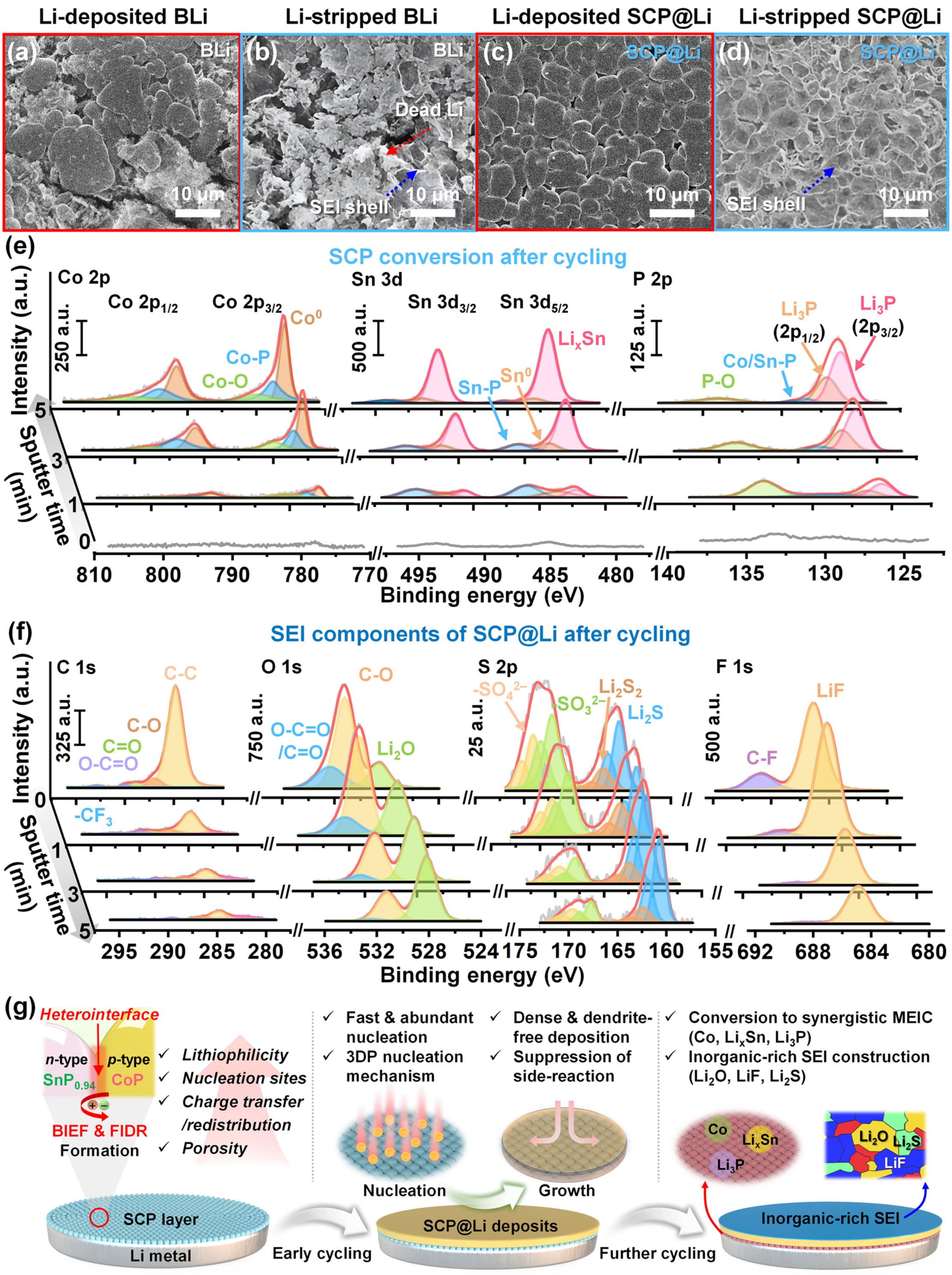

Fig. 5 Analysis of morphology and chemical composition after cycling. SEM images of **a** Li-deposited BLi, **b** Li-stripped BLi, **c** Li-deposited SCP@Li, and **d** Li-stripped SCP@Li after 50 cycles at a current density of 1 mA cm^{-2} under a capacity of 1 mAh cm^{-2}. **e** Depth-profiled XPS spectra of SCP modulation layer in SCP@Li after cycling. **f** Depth-profiled XPS spectra of SEI on SCP@Li after cycling. **g** Schematic illustration of comprehensive Li deposition mechanism during cycling of SCP modulation layer

sputtering. This implies that the SEI thickness was thinner than the BLi [96]. Similar to the trend of the C 1*s* spectra, with the increase in Ar^+ sputtering time, the O 1*s* and S 2*p* spectra of SCP@Li also demonstrate a gradual decrease in organic species corresponding to C–O (531.2 eV), C=O/O–C=O (532.3 eV), $-SO_4^{2-}$ ($2p_{1/2}$: 170.2 eV, $2p_{3/2}$: 169.1 eV), and $-SO_3^{2-}$ ($2p_{1/2}$: 168.3 eV, $2p_{3/2}$: 167.1 eV) that is more rapid than that of BLi. Significantly, the inner SEI of SCP@Li is predominantly composed of inorganic Li_2O (528.5 eV), Li_2S_2 ($2p_{1/2}$: 163.1 eV eV, $2p_{3/2}$: 161.9 eV), and Li_2S ($2p_{1/2}$: 161.4 eV eV, $2p_{3/2}$: 160.2 eV), rather than organic species [95, 96]. For the F 1*s* spectra, two typical peaks corresponding to C-F (688.5 eV, originated from LiTFSI remnants) and LiF (685.1 eV, originated from the decomposition of LiTFSI) are observed [97]. Unlike BLi, where the LiF peak maintains a high intensity notwithstanding the increase in etching depth, the reducing LiF peak intensity in SCP@Li with progressive etching depth indicates that the altered dense Li deposition behavior of SCP@Li can suppress the decomposition of LiTFSI. Based on an XPS depth profiling analysis, the calculated atomic proportions of SEIs on SCP@Li and BLi further strengthen that SCP@Li facilitates the formation of an inorganic-rich SEI, unlike BLi (Fig. S37) [98, 99]. These inorganic components provide various advantages. First, the abundance of Li_2O plays a crucial role in the development of compact SEI [100]. Second, Li_xS components can facilitate enhanced Li-ion diffusion and uniform distribution of Li-ion flux, whereas LiF can increase the mechanical stability and lower the diffusion barrier [101, 102].

Synthesizing these observations, the Li deposition mechanism of the SCP modulation layer is summarized comprehensively (Fig. 5g). During the early Li plating/stripping process, owing to the favorable heterostructure (lithiophilic heterointerface, abundant nucleation sites and enhanced charge redistribution) of the SCP, Li nucleation and growth can be significantly uniform and compact without Li dendrites and protrusions while suppressing side reactions with the electrolyte. As successive cycles proceed, the spontaneous conversion of SCP into Co, Li_xSn, and Li_3P composites induced by the spontaneous reaction with metallic Li and the construction of an inorganic-rich SEI play crucial roles in maintaining a stable Li plating/stripping process over long-term cycles.

3.6 Full Cell Performance Evaluation of SCP@Li

To assess the practical application of SCP@Li in full cells, we examined the feasibility of incorporating SCP@Li into full cells combined with NCM811 cathodes. The CV curves across scan rates (0.1–1.0 mV s^{-1}) revealed that the NCM811//SCP@Li cell exhibits more obvious anodic (A1) and cathodic (C1) peaks with higher redox current densities and smaller voltage separation between A1 and C1 peaks (360 mV for NCM811//SCP@Li cell and 580 mV for NCM811//BLi cell) than the NCM811//BLi cell (Fig. 6a, b). This reflects the reduced polarization and enhanced electrochemical reactivity of NCM811//SCP@Li cell. Furthermore, the Li-ion transfer kinetics were analyzed based on the Li-ion diffusion coefficients (D_{Li^+}) using the Randles–Sevcik equation. As shown in Fig. 6c, the A1 and C1 peaks at various scan rates exhibit a linearly proportional relationship with the square root of the voltage scan rates. This indicates a diffusion-controlled electrochemical process in the full cells. The calculated D_{Li^+} values of the NCM811//SCP@Li cell for the A1 and C1 peaks were 2.29×10^{-8} and 1.16×10^{-8} $cm^2\ s^{-1}$, respectively. These are higher than those of NCM811//BLi cell (A1 peak: 1.19×10^{-8} $cm^2\ s^{-1}$, C1 Peak: 4.71×10^{-9} $cm^2\ s^{-1}$). The result agrees with the outstanding electrochemical kinetics, thereby demonstrating an accelerated Li-ion desolvation effect and enhanced Li-ion transportation, as discussed in Fig. 3.

The rate performances of the NCM811//SCP@Li and NCM811//BLi cells were measured at various C-rates (Fig. 6d). Apparently, with stepwise C-rates from 0.2 C to 5 C, the specific discharge capacities of the NCM811//SCP@Li are 184.8, 166.5, 153.7, 125.6, 103.4, and 72.2 mAh g^{-1}, respectively. These distinctly surpass the capacities measured for the NCM811//BLi cell (175.3, 146.5, 108.9, 73.2, 53.9, and 21.3 mAh g^{-1}). In addition, NCM811//SCP@Li retained its original specific capacity as the C-rate returned to 0.5 C again. Moreover, the galvanostatic profiles of the NCM811//SCP@Li cell clearly demonstrate overpotentials less than those of NCM811/BLi cell (Fig. S38), indicating the improved rate capability and redox kinetics across current densities. Regarding durability, the NCM811//SCP@Li full cell displayed a higher initial capacity (165.7 mAh g^{-1}) and excellent capacity retention (~49.3%), outperforming those of the NCM811//BLi full cell (initial capacity:

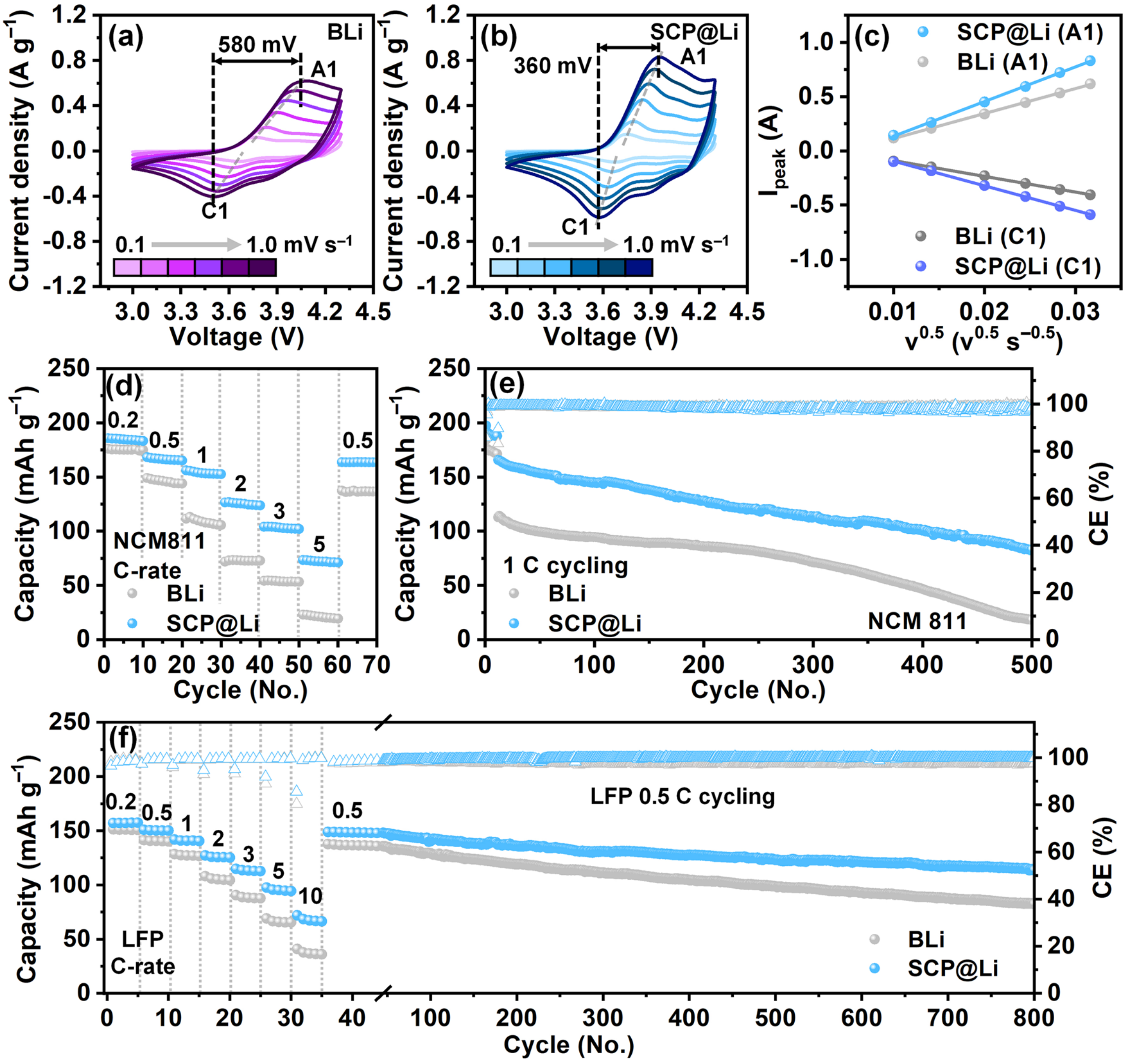

Fig. 6 Full cell performance evaluation of SCP@Li. CV curves of **a** NCM811//BLi and **b** NCM811//SCP@Li across the scan rates, and **c** the corresponding linear fit of the cathodic/anodic peak current intensities as a function of the square root of the scan rates. **d** Rate performance and **e** cycling performance of NCM811//BLi and NCM811//SCP@Li cells. **f** Rate performance and subsequent cycling performance of LFP//BLi and LFP//SCP@Li cells

114.2 mAh g^{-1}, capacity retention: ~15.9%) after 500 cycles at 1 C (Fig. 6e). To further demonstrate the potential of SCP@Li for practical use, LFP full cells with SCP@Li and BLi anodes were subjected to cycling tests combined with C-rate and subsequent long-term galvanostatic cycling. As anticipated (Fig. 6f and Table S4), the LFP//SCP@Li cell displayed improved rate capability and long-term cycling stability (initial capacity: 148.9 mAh g^{-1}, capacity retention: ~75.8%) at 0.5 C compared with the LFP//BLi cell (initial capacity: 137.7 mAh g^{-1}, capacity retention: ~59.1%).

4 Conclusion

To summarize, we proposed a pioneering design for a modulation layer composed of a highly lithiophilic CoP/$SnP_{0.94}$ heterostructure applying the Kirkendall effect. During the initial cycling, the spontaneous FIDR and BIEF formation of the *p*–*n* junction in the SCP provided abundant lithiophilic nucleation sites and enhanced charge transfer, as demonstrated by experiments and theoretical calculations. This induced a uniform Li nucleation/growth behavior with the suppression of volume expansion, Li dendrite formation, and

https://doi.org/10.1007/s40820-025-01813-1

electrolyte consumption. As revealed by XPS depth profiling analysis, with continuous cycling, the progressive transformation of SCP into the MEIC layer (consisting of metallic Co, lithiophilic Li-Sn alloy, and high ionic conductive Li_3P) and development of inorganic-rich SEI layer enables the initial stable Li deposition behavior of SCP@Li to persist for long-term cycling. As result, SCP@Li demonstrated superior electrochemical kinetics and performance, including a high ionic conductivity, high exchange current density, and remarkable cycling stability for 750 cycles while sustaining a low overpotential of 68 mV in the symmetric cell test, even at a high current density of 5 mA cm^{-2}. Moreover, the LFP//SCP@Li full cell delivered a high-capacity retention of 75.8% for 800 cycles at 0.5 C. This work has revealed the regulatory role of lithiophilic heterostructures on Li deposition behavior and the role of compositional transition in artificial SEI during cycling. This provides a meaningful reference for designing of highly effective modulation layers for LMAs.

Acknowledgements This work was supported by the Basic Science Research Program through National Research Foundation of Korea (NRF) grant funded by the Ministry of Education (RS-2020-NR049594) and the Ministry of Science and ICT (RS-2022-NR070534).

Author Contributions Jung Been Park was involved in writing—original draft, conceptualization, data curation, investigation, methodology, project administration, validation, and visualization. Changhoon Choi was involved in writing—original draft, conceptualization, methodology, project administration, and validation. Min Sang Kim was involved in software, formal analysis, and investigation. Hyeongbeom Kang was involved in formal analysis and investigation. Eunji Kang was involved in software and formal analysis. Seungho Yu was involved in software and formal analysis. Dong-Wan Kim was involved in writing—review and editing, conceptualization, resources, project administration, supervision, validation, and funding acquisition.

Declarations

Conflict of interest The authors declare no interest conflict of interest. They have no known competing financial interests or personal relationships that could have appeared to influence the work reported in this paper.

Supplementary Information The online version contains supplementary material available at https://doi.org/10.1007/s40820-025-01813-1.

References

1. J. Lin, X. Zhang, E. Fan, R. Chen, F. Wu et al., Carbon neutrality strategies for sustainable batteries: from structure, recycling, and properties to applications. Energy Environ. Sci. **16**(3), 745–791 (2023). https://doi.org/10.1039/D2EE03257K
2. Y. Gao, Z. Pan, J. Sun, Z. Liu, J. Wang, High-energy batteries: beyond lithium-ion and their long road to commercialisation. Nano-Micro Lett. **14**(1), 94 (2022). https://doi.org/10.1007/s40820-022-00844-2
3. M. Li, J. Lu, Z. Chen, K. Amine, 30 years of lithium-ion batteries. Adv. Mater. **30**, e1800561 (2018). https://doi.org/10.1002/adma.201800561
4. B.C. Min, J.B. Park, C. Choi, D.-W. Kim, Dynamic construction of a composite solid electrolyte interphase for dendrite-free lithium metal batteries *via* lithium-antimony self-alloying. Adv. Compos. Hybrid Mater. **8**(1), 4 (2024). https://doi.org/10.1007/s42114-024-01070-7
5. J.B. Park, C. Choi, S. Yu, K.Y. Chung, D.-W. Kim, Porous lithiophilic Li–Si alloy-type interfacial framework *via* self-discharge mechanism for stable lithium metal anode with superior rate. Adv. Energy Mater. **11**(37), 2170146 (2021). https://doi.org/10.1002/aenm.202170146
6. Y. Li, W. Huang, Y. Li, A. Pei, D.T. Boyle et al., Correlating structure and function of battery interphases at atomic resolution using cryoelectron microscopy. Joule **2**(10), 2167–2177 (2018). https://doi.org/10.1016/j.joule.2018.08.004
7. T. Zhao, S. Li, F. Liu, Z. Wang, H. Wang et al., Molten-Li infusion of ultra-thin interfacial modification layer towards the highly-reversible, energy-dense metallic batteries. Energy Storage Mater. **45**, 796–804 (2022). https://doi.org/10.1016/j.ensm.2021.12.032
8. X. Zhang, Y. Yang, Z. Zhou, Towards practical lithium-metal anodes. Chem. Soc. Rev. **49**(10), 3040–3071 (2020). https://doi.org/10.1039/c9cs00838a
9. W. Xu, J. Wang, F. Ding, X. Chen, E. Nasybulin et al., Lithium metal anodes for rechargeable batteries. Energy Environ. Sci. **7**(2), 513–537 (2014). https://doi.org/10.1039/C3EE40795K
10. H. Xiao, X. Li, Y. Fu, Advances in anion chemistry in the electrolyte design for better lithium batteries.

Nano-Micro Lett. **17**(1), 149 (2025). https://doi.org/10.1007/s40820-024-01629-5

11. J. Chen, X. Fan, Q. Li, H. Yang, M.R. Khoshi et al., Electrolyte design for LiF-rich solid–electrolyte interfaces to enable high-performance microsized alloy anodes for batteries. Nat. Energy **5**(5), 386–397 (2020). https://doi.org/10.1038/s41560-020-0601-1
12. Z. Fan, X. Chen, J. Shi, H. Nie, X. Zhang et al., Functionalized separators boosting electrochemical performances for lithium batteries. Nano-Micro Lett. **17**(1), 128 (2025). https://doi.org/10.1007/s40820-024-01596-x
13. S. Ye, X. Chen, R. Zhang, Y. Jiang, F. Huang et al., Revisiting the role of physical confinement and chemical regulation of 3D hosts for dendrite-free Li metal anode. Nano-Micro Lett. **14**(1), 187 (2022). https://doi.org/10.1007/s40820-022-00932-3
14. T. Zhu, Z. Li, Z. Chen, E. Hu, L. Wang et al., Lithiophilic hollow $Co_3[Co(CN)_6]_2$ embedded carbon nanotube film for dendrite-free lithium metal anodes. J. Colloid Interface Sci. **623**, 532–540 (2022). https://doi.org/10.1016/j.jcis.2022.05.055
15. X. Zhang, S. Cheng, C. Fu, G. Yin, L. Wang et al., Advancements and challenges in organic-inorganic composite solid electrolytes for all-solid-state lithium batteries. Nano-Micro Lett. **17**(1), 2 (2024). https://doi.org/10.1007/s40820-024-01498-y
16. L. He, Q. Sun, C. Chen, J.A.S. Oh, J. Sun et al., Failure mechanism and interface engineering for NASICON-structured all-solid-state lithium metal batteries. ACS Appl. Mater. Interfaces **11**(23), 20895–20904 (2019). https://doi.org/10.1021/acsami.9b05516
17. X. Xu, X. Yue, Y. Chen, Z. Liang, Li plating regulation on fast-charging graphite anodes by a triglyme-$LiNO_3$ synergistic electrolyte additive. Angew. Chem. Int. Ed. **62**(34), e202306963 (2023). https://doi.org/10.1002/anie.202306963
18. E. Markevich, G. Salitra, F. Chesneau, M. Schmidt, D. Aurbach, Very stable lithium metal stripping–plating at a high rate and high areal capacity in fluoroethylene carbonate-based organic electrolyte solution. ACS Energy Lett. **2**(6), 1321–1326 (2017). https://doi.org/10.1021/acsenergylett.7b00300
19. X. Li, J. Liu, J. He, S. Qi, M. Wu et al., Separator-wetted, acid- and water-scavenged electrolyte with optimized Li-ion solvation to form dual efficient electrode electrolyte interphases *via* hexa-functional additive. Adv. Sci. **9**(20), e2201297 (2022). https://doi.org/10.1002/advs.202201297
20. G. Guo, K. Zhang, K. Zhu, P. Yang, Z. Shao et al., Refined pore structure design and surface modification of 3D porous copper achieving highly stable dendrite-free lithium-metal anode. Adv. Funct. Mater. **34**(38), 2402490 (2024). https://doi.org/10.1002/adfm.202402490
21. A. Huang, Y. Wu, H. Huang, C. Li, Y. Sun et al., Lithiophilic Mo_2C clusters-embedded carbon nanofibers for high energy density lithium metal batteries. Adv. Funct. Mater. **33**(36), 2303111 (2023). https://doi.org/10.1002/adfm.202303111
22. W. Wu, D. Ning, J. Zhang, G. Liu, L. Zeng et al., Ultralight lithiophilic three-dimensional lithium host for stable high-energy-density anode-free lithium metal batteries. Energy Storage Mater. **63**, 102974 (2023). https://doi.org/10.1016/j.ensm.2023.102974
23. Q. Li, S. Zhu, Y. Lu, 3D porous Cu current collector/Li-metal composite anode for stable lithium-metal batteries. Adv. Funct. Mater. **27**(18), 1606422 (2017). https://doi.org/10.1002/adfm.201606422
24. D. Chen, C. Chen, H. Yu, S. Zheng, T. Jin et al., Formation of N-doped carbon nanofibers decorated with MoP nanoflakes for dendrite-free lithium metal anode. Adv. Funct. Mater. **34**(38), 2402951 (2024). https://doi.org/10.1002/adfm.202402951
25. Y. Zhang, C. Wang, G. Pastel, Y. Kuang, H. Xie et al., 3D wettable framework for dendrite-free alkali metal anodes. Adv. Energy Mater. **8**(18), 1800635 (2018). https://doi.org/10.1002/aenm.201800635
26. Z.-X. Wang, Y. Lu, C.-Z. Zhao, W.-Z. Huang, X.-Y. Huang et al., Suppressing Li voids in all-solid-state lithium metal batteries through Li diffusion regulation. Joule **8**(10), 2794–2810 (2024). https://doi.org/10.1016/j.joule.2024.07.007
27. Y.-L. Liao, X.-L. Wang, H. Yuan, Y.-J. Li, C.-M. Xu et al., Ultrafast Li-rich transport in composite solid-state electrolytes. Adv. Mater. **37**(10), e2419782 (2025). https://doi.org/10.1002/adma.202419782
28. X. Gao, Y. Chen, Z. Zhen, L. Cui, L. Huang et al., Construction of multifunctional conductive carbon-based cathode additives for boosting Li_6PS_5Cl-based all-solid-state lithium batteries. Nano-Micro Lett. **17**(1), 140 (2025). https://doi.org/10.1007/s40820-025-01667-7
29. P. Albertus, S. Babinec, S. Litzelman, A. Newman, Status and challenges in enabling the lithium metal electrode for high-energy and low-cost rechargeable batteries. Nat. Energy **3**(1), 16–21 (2017). https://doi.org/10.1038/s41560-017-0047-2
30. Z. Luo, S. Li, L. Yang, Y. Tian, L. Xu et al., Interfacially Redistributed charge for robust lithium metal anode. Nano Energy **87**, 106212 (2021). https://doi.org/10.1016/j.nanoen.2021.106212
31. Z. Tu, S. Choudhury, M.J. Zachman, S. Wei, K. Zhang et al., Designing artificial solid-electrolyte interphases for single-ion and high-efficiency transport in batteries. Joule **1**(2), 394–406 (2017). https://doi.org/10.1016/j.joule.2017.06.002
32. X.-B. Cheng, C. Yan, X.-Q. Zhang, H. Liu, Q. Zhang, Electronic and ionic channels in working interfaces of lithium metal anodes. ACS Energy Lett. **3**(7), 1564–1570 (2018). https://doi.org/10.1021/acsenergylett.8b00526
33. Z. Chang, Y. Qiao, H. Deng, H. Yang, P. He et al., A liquid electrolyte with de-solvated lithium ions for lithium-metal battery. Joule **4**(8), 1776–1789 (2020). https://doi.org/10.1016/j.joule.2020.06.011
34. Y. Chen, M. He, N. Zhao, J. Fu, H. Huo et al., Nanocomposite intermediate layers formed by conversion reaction of SnO_2 for Li/garnet/Li cycle stability. J. Power. Sources **420**, 15–21 (2019). https://doi.org/10.1016/j.jpowsour.2019.02.085

35. X. Qiu, M. Yu, G. Fan, J. Liu, Y. Wang et al., Growing nanostructured CuO on copper foil *via* chemical etching to upgrade metallic lithium anode. ACS Appl. Mater. Interfaces **13**(5), 6367–6374 (2021). https://doi.org/10.1021/acsami.0c22046
36. D. Xie, H.-H. Li, W.-Y. Diao, R. Jiang, F.-Y. Tao et al., Spatial confinement of vertical arrays of lithiophilic SnS_2 nanosheets enables conformal Li nucleation/growth towards dendrite-free Li metal anode. Energy Storage Mater. **36**, 504–513 (2021). https://doi.org/10.1016/j.ensm.2021.01.034
37. S. Li, Q. Liu, J. Zhou, T. Pan, L. Gao et al., Hierarchical Co_3O_4 nanofiber–carbon sheet skeleton with superior Na/Li-philic property enabling highly stable alkali metal batteries. Adv. Funct. Mater. **29**(19), 1808847 (2019). https://doi.org/10.1002/adfm.201808847
38. C. Sun, A. Lin, W. Li, J. Jin, Y. Sun et al., *In situ* conversion of Cu_3P nanowires to mixed ion/electron-conducting skeleton for homogeneous lithium deposition. Adv. Energy Mater. **10**(3), 1902989 (2020). https://doi.org/10.1002/aenm.201902989
39. C. Zhang, R. Lyu, W. Lv, H. Li, W. Jiang et al., A lightweight 3D Cu nanowire network with phosphidation gradient as current collector for high-density nucleation and stable deposition of lithium. Adv. Mater. **31**(48), 1904991 (2019). https://doi.org/10.1002/adma.201904991
40. H. Jiang, H. Fan, Z. Han, B. Hong, F. Wu et al., A 3D conducting scaffold with *in situ* grown lithiophilic Ni_2P nanoarrays for high stability lithium metal anodes. J. Energy Chem. **54**, 301–309 (2021). https://doi.org/10.1016/j.jechem.2020.06.004
41. C. Fu, S. Lin, C. Zhao, J. Wang, L. Wang et al., Li migration, nucleation and growth behavior regulated by a lithiophilic cobalt phosphide-doped carbon nanofibers derived ion/electron conductive framework. Energy Storage Mater. **45**, 1109–1119 (2022). https://doi.org/10.1016/j.ensm.2021.11.009
42. X. Zhang, S. Jin, M.H. Seo, C. Shang, G. Zhou et al., Hierarchical porous structure construction for highly stable self-supporting lithium metal anode. Nano Energy **93**, 106905 (2022). https://doi.org/10.1016/j.nanoen.2021.106905
43. L. Lin, F. Liang, K. Zhang, H. Mao, J. Yang et al., Lithium phosphide/lithium chloride coating on lithium for advanced lithium metal anode. J. Mater. Chem. A **6**(32), 15859–15867 (2018). https://doi.org/10.1039/C8TA05102J
44. Y. Li, J. Zhang, Q. Chen, X. Xia, M. Chen, Emerging of heterostructure materials in energy storage: a review. Adv. Mater. **33**(27), 2100855 (2021). https://doi.org/10.1002/adma.202100855
45. Z. Hao, D. Liu, X. Zuo, H. Yu, T. You et al., Built-In electric field induced uniform Li deposition *via* construction of CoP/Co_2P heterojunction in 3D carbon nanofiber networks. Adv. Funct. Mater. **35**(7), 2415251 (2025). https://doi.org/10.1002/adfm.202415251
46. X. Shen, S. Shi, B. Li, S. Li, H. Zhang et al., Lithiophilic interphase porous buffer layer toward uniform nucleation in lithium metal anodes. Adv. Funct. Mater. **32**(39), 2206388 (2022). https://doi.org/10.1002/adfm.202206388
47. Y. Yang, E. Hu, Y. Zhu, W. Cao, J. Zhang et al., A flexible carbon nanotube film modified with gradient lithiophilic Cu_2O/Cu heterojunction for dendrite-free lithium metal anodes. Chem. Eng. J. **477**, 146879 (2023). https://doi.org/10.1016/j.cej.2023.146879
48. Y. Zhu, Y. Yang, H. Zhang, S. Liu, Z. Wu et al., A highly-lithiophilic Mn_3O_4/ZnO-modified carbon nanotube film for dendrite-free lithium metal anodes. J. Colloid Interface Sci. **648**, 299–307 (2023). https://doi.org/10.1016/j.jcis.2023.05.101
49. Q. Meng, M. Guan, Y. Huang, L. Li, F. Wu et al., Multi-dimensional Co_3O_4/NiO heterojunctions with rich-boundaries incorporated into reduced graphene oxide network for expanding the range of lithiophilic host. InfoMat **4**(8), e12313 (2022). https://doi.org/10.1002/inf2.12313
50. L. Ruan, X. Qin, K. Lin, Z. Yang, Q. Cai et al., TiO_2/Cu_2O heterostructure enabling selective and uniform lithium deposition towards stable lithium metal anodes. Nano Res. **16**(4), 4917–4925 (2023). https://doi.org/10.1007/s12274-022-5066-z
51. T. Le, C. Yang, W. Lv, Q. Liang, X. Huang et al., Deeply cyclable and ultrahigh-rate lithium metal anodes enabled by coaxial nanochamber heterojunction on carbon nanofibers. Adv. Sci. **8**(23), 2101940 (2021). https://doi.org/10.1002/advs.202101940
52. X. Fan, T. Gao, C. Luo, F. Wang, J. Hu et al., Superior reversible tin phosphide-carbon spheres for sodium ion battery anode. Nano Energy **38**, 350–357 (2017). https://doi.org/10.1016/j.nanoen.2017.06.014
53. D. Liu, X. Li, L. Wei, T. Zhang, A. Wang et al., Disproportionation of hypophosphite and phosphite. Dalton Trans. **46**(19), 6366–6378 (2017). https://doi.org/10.1039/c7dt00243b
54. J.B. Park, C. Choi, J.H. Park, S. Yu, D.-W. Kim, Synergistic design of multifunctional interfacial Zn host toward practical Zn metal batteries. Adv. Energy Mater. **12**(48), 2202937 (2022). https://doi.org/10.1002/aenm.202202937
55. J. Zhang, X. Liang, X. Wang, Z. Zhuang, CoP nanotubes formed by Kirkendall effect as efficient hydrogen evolution reaction electrocatalysts. Mater. Lett. **202**, 146–149 (2017). https://doi.org/10.1016/j.matlet.2017.04.154
56. S. Huang, C. Meng, M. Xiao, S. Ren, S. Wang et al., Multi-shell tin phosphide nanospheres as high performance anode material for a sodium ion battery. Sustain. Energy Fuels **1**(9), 1944–1949 (2017). https://doi.org/10.1039/C7SE00355B
57. J. Chang, Y. Xiao, M. Xiao, J. Ge, C. Liu et al., Surface oxidized cobalt-phosphide nanorods as an advanced oxygen evolution catalyst in alkaline solution. ACS Catal. **5**(11), 6874–6878 (2015). https://doi.org/10.1021/acscatal.5b02076
58. S. Liu, K. Feng, W. Xu, J. Tong, Study on tin-cobalt bimetallic phosphide nanoparticles as a negative electrode of sodium-ion batteries. Langmuir **40**(19), 10270–10280 (2024). https://doi.org/10.1021/acs.langmuir.4c00794

59. R. Liang, Y. Wang, C. Qin, X. Chen, Z. Ye et al., P-type cobalt phosphide composites (CoP-Co_2P) decorated on titanium oxide for enhanced noble-metal-free photocatalytic H_2 evolution activity. Langmuir **37**(11), 3321–3330 (2021). https://doi.org/10.1021/acs.langmuir.0c03362
60. W. Zhang, N. Han, J. Luo, X. Han, S. Feng et al., Critical role of phosphorus in hollow structures cobalt-based phosphides as bifunctional catalysts for water splitting. Small **18**(4), e2103561 (2022). https://doi.org/10.1002/smll.202103561
61. X. Zhao, W. Wang, Z. Hou, G. Wei, Y. Yu et al., $SnP_{0.94}$ nanoplates/graphene oxide composite for novel potassium-ion battery anode. Chem. Eng. J. **370**, 677–683 (2019). https://doi.org/10.1016/j.cej.2019.03.250
62. V. Tallapally, R.J.A. Esteves, L. Nahar, I.U. Arachchige, Multivariate synthesis of tin phosphide nanoparticles: temperature, time, and ligand control of size, shape, and crystal structure. Chem. Mater. **28**(15), 5406–5414 (2016). https://doi.org/10.1021/acs.chemmater.6b01749
63. Y. Kim, H. Hwang, C.S. Yoon, M.G. Kim, J. Cho, Reversible lithium intercalation in teardrop-shaped ultrafine $SnP_{0.94}$ particles: an anode material for lithium-ion batteries. Adv. Mater. **19**(1), 92–96 (2007). https://doi.org/10.1002/adma.200600644
64. L. Häggström, J. Gullman, T. Ericsson, R. Wäppling, Mössbauer study of tin phosphides. J. Solid State Chem. **13**(3), 204–207 (1975). https://doi.org/10.1016/0022-4596(75)90120-6
65. Z. Song, Y. Liu, Z. Wang, J. Xing, C. Wei et al., Synergistic modulation of Li nucleation/growth enabled by CNTs-wrapped lithiophilic CoP/Co_2P decorated hollow carbon polyhedron host for stable lithium metal anodes. Nano Res. **16**(4), 4961–4969 (2023). https://doi.org/10.1007/s12274-022-5179-4
66. C.-T. Sah, R.N. Noyce, W. Shockley, Carrier generation and recombination in P-N junctions and P-N junction characteristics. Proc. IRE **45**(9), 1228–1243 (1957). https://doi.org/10.1109/JRPROC.1957.278528
67. S.C. Choo, Carrier generation-recombination in the space-charge region of an asymmetrical *p-n* junction. Solid State Electron. **11**(11), 1069–1077 (1968). https://doi.org/10.1016/0038-1101(68)90129-9
68. P. Zhai, T. Wang, H. Jiang, J. Wan, Y. Wei et al., 3D artificial solid-electrolyte interphase for lithium metal anodes enabled by insulator–metal–insulator layered heterostructures. Adv. Mater. **33**(13), 2006247 (2021). https://doi.org/10.1002/adma.202006247
69. Y. Li, Y. Li, A. Pei, K. Yan, Y. Sun et al., Atomic structure of sensitive battery materials and interfaces revealed by cryo-electron microscopy. Science **358**(6362), 506–510 (2017). https://doi.org/10.1126/science.aam6014
70. Z. Wu, C. Wang, Z. Hui, H. Liu, S. Wang et al., Growing single-crystalline seeds on lithiophobic substrates to enable fast-charging lithium-metal batteries. Nat. Energy **8**(4), 340–350 (2023). https://doi.org/10.1038/s41560-023-01202-1
71. B.R. Scharifker, J. Mostany, Three-dimensional nucleation with diffusion controlled growth Part I. Number density of active sites and nucleation rates per site. J. Electroanal. Chem. Interfacial Electrochem. **177**(1–2), 13–23 (1984). https://doi.org/10.1016/0022-0728(84)80207-7
72. W. To-A-Ran, N.R. Mastoi, C.Y. Ha, Y.J. Song, Y.J. Kim, Kelvin probe force microscopy and electrochemical atomic force microscopy investigations of lithium nucleation and growth: influence of the electrode surface potential. J. Phys. Chem. Lett. **15**(28), 7265–7271 (2024). https://doi.org/10.1021/acs.jpclett.4c01148
73. B. Thirumalraj, T.T. Hagos, C.-J. Huang, M.A. Teshager, J.-H. Cheng et al., Nucleation and growth mechanism of lithium metal electroplating. J. Am. Chem. Soc. **141**(46), 18612–18623 (2019). https://doi.org/10.1021/jacs.9b10195
74. B. Scharifker, G. Hills, Theoretical and experimental studies of multiple nucleation. Electrochim. Acta **28**(7), 879–889 (1983). https://doi.org/10.1016/0013-4686(83)85163-9
75. Y. Zhao, S. Guo, M. Chen, B. Lu, X. Zhang et al., Tailoring grain boundary stability of zinc-titanium alloy for long-lasting aqueous zinc batteries. Nat. Commun. **14**, 7080 (2023). https://doi.org/10.1038/s41467-023-42919-7
76. W. Tang, T. Zhao, K. Wang, T. Yu, R. Lv et al., Dendrite-free lithium metal batteries enabled by coordination chemistry in polymer-ceramic modified separators. Adv. Funct. Mater. **34**(18), 2314045 (2024). https://doi.org/10.1002/adfm.202314045
77. P. Xu, X. Hu, X. Liu, X. Lin, X. Fan et al., A lithium-metal anode with ultra-high areal capacity (50 mAh Cm−2) by gridding lithium plating/stripping. Energy Storage Mater. **38**, 190–199 (2021). https://doi.org/10.1016/j.ensm.2021.03.010
78. Y. Liu, W. Guan, S. Li, J. Bi, X. Hu et al., Sustainable dual-layered interface for long-lasting stabilization of lithium metal anodes. Adv. Energy Mater. **13**(48), 2302695 (2023). https://doi.org/10.1002/aenm.202302695
79. Z. Fu, G. Xia, J. Ye, Z. Zheng, J. Wang et al., A modified separator based on ternary mixed-oxide for stable lithium metal batteries. J. Colloid Interface Sci. **679**, 830–839 (2025). https://doi.org/10.1016/j.jcis.2024.10.127
80. Y. Wang, F. Liu, G. Fan, X. Qiu, J. Liu et al., Electroless formation of a fluorinated Li/Na hybrid interphase for robust lithium anodes. J. Am. Chem. Soc. **143**(7), 2829–2837 (2021). https://doi.org/10.1021/jacs.0c12051
81. Z. Hao, C. Wang, Y. Wu, Q. Zhang, H. Xu et al., Electronegative nanochannels accelerating lithium-ion transport for enabling highly stable and high-rate lithium metal anodes. Adv. Energy Mater. **13**(28), 2204007 (2023). https://doi.org/10.1002/aenm.202204007
82. G. Lin, K. Jia, Z. Bai, C. Liu, S. Liu et al., Metal-organic framework sandwiching porous super-engineering polymeric membranes as anionphilic separators for dendrite-free lithium metal batteries. Adv. Funct. Mater. **32**(47), 2207969 (2022). https://doi.org/10.1002/adfm.202207969
83. K. Jang, H.J. Song, J.B. Park, S.W. Jung, D.-W. Kim, Magnesium fluoride-engineered UiO-66 artificial protection layers for dendrite-free lithium metal batteries. Energy Environ. Sci. **17**(13), 4622–4633 (2024). https://doi.org/10.1039/D4EE01428F

84. D. Kang, N. Hart, M. Xiao, J.P. Lemmon, Short circuit of symmetrical Li/Li cell in Li metal anode research. Acta Phys. Chim. Sin. **37**(2), 2008013 (2021). https://doi.org/10.3866/pku.whxb202008013
85. P. Yadav, W. Malik, P.K. Dwivedi, L.A. Jones, M.V. Shelke, Electrospun nanofibers of tin phosphide ($SnP_{0.94}$) nanoparticles encapsulated in a carbon matrix: a tunable conversion-cum-alloying lithium storage anode. Energy Fuels **34**(6), 7648–7657 (2020). https://doi.org/10.1021/acs.energyfuels.0c01046
86. H. Wang, D. Lin, J. Xie, Y. Liu, H. Chen et al., An interconnected channel-like framework as host for lithium metal composite anodes. Adv. Energy Mater. **9**(7), 1802720 (2019). https://doi.org/10.1002/aenm.201802720
87. C. Fu, H. Yang, P. Jia, C. Zhao, L. Wang et al., Steady cycling of lithium metal anode enabled by alloying Sn-modified carbon nanofibers. J. Mater. Chem. A **11**(28), 15237–15245 (2023). https://doi.org/10.1039/D3TA02379F
88. X. Xiong, W. Yan, Y. Zhu, L. Liu, L. Fu et al., $Li_4Ti_5O_{12}$ coating on copper foil as ion redistributor layer for stable lithium metal anode. Adv. Energy Mater. **12**(13), 2103112 (2022). https://doi.org/10.1002/aenm.202103112
89. X. Cao, Y. Xu, L. Zou, J. Bao, Y. Chen et al., Stability of solid electrolyte interphases and calendar life of lithium metal batteries. Energy Environ. Sci. **16**(4), 1548–1559 (2023). https://doi.org/10.1039/D2EE03557J
90. C. Hu, Y. Hu, A. Chen, X. Duan, H. Jiang et al., Atomic interface catalytically synthesizing SnP/CoP hetero-nanocrystals within dual-carbon hybrids for ultrafast lithium-ion batteries. Engineering **18**, 154–160 (2022). https://doi.org/10.1016/j.eng.2021.11.026
91. K.K.D. Ehinon, S. Naille, R. Dedryvère, P.-E. Lippens, J.-C. Jumas et al., Ni_3Sn_4 electrodes for Li-ion batteries: Li–Sn alloying process and electrode/electrolyte interface phenomena. Chem. Mater. **20**(16), 5388–5398 (2008). https://doi.org/10.1021/cm8006099
92. S.-H. Hwang, S.-D. Seo, D.-W. Kim, A novel time-saving synthesis approach for Li-argyrodite superionic conductor. Adv. Sci. **10**(22), e2301707 (2023). https://doi.org/10.1002/advs.202301707
93. W. Li, S. Zheng, Y. Gao, D. Feng, Y. Ru et al., High rate and low-temperature stable lithium metal batteries enabled by lithiophilic 3D Cu-CuSn porous framework. Nano Lett. **23**(17), 7805–7814 (2023). https://doi.org/10.1021/acs.nanolett.3c01266
94. L. Lin, L. Suo, Y.-S. Hu, H. Li, X. Huang et al., Epitaxial induced plating current-collector lasting lifespan of anode-free lithium metal battery. Adv. Energy Mater. **11**(9), 2003709 (2021). https://doi.org/10.1002/aenm.202003709
95. C. Chen, Q. Liang, G. Wang, D. Liu, X. Xiong, Grain-boundary-rich artificial SEI layer for high-rate lithium metal anodes. Adv. Funct. Mater. **32**(4), 2107249 (2022). https://doi.org/10.1002/adfm.202107249
96. F. Chu, R. Deng, F. Wu, Unveiling the effect and correlative mechanism of series-dilute electrolytes on lithium metal anodes. Energy Storage Mater. **56**, 141–154 (2023). https://doi.org/10.1016/j.ensm.2023.01.001
97. S. Yuan, S. Weng, F. Wang, X. Dong, Y. Wang et al., Revisiting the designing criteria of advanced solid electrolyte interphase on lithium metal anode under practical condition. Nano Energy **83**, 105847 (2021). https://doi.org/10.1016/j.nanoen.2021.105847
98. S.-J. Yang, H. Yuan, N. Yao, J.-K. Hu, X.-L. Wang et al., Intrinsically safe lithium metal batteries enabled by thermo-electrochemical compatible *in situ* polymerized solid-state electrolytes. Adv. Mater. **36**(35), 2405086 (2024). https://doi.org/10.1002/adma.202405086
99. X.-L. Wang, Y. Li, J. Liu, S.-J. Yang, J.-K. Hu et al., A robust dual-layered solid electrolyte interphase enabled by cation specific adsorption-induced built-In electrostatic field for long-cycling solid-state lithium metal batteries. Angew. Chem. Int. Ed. **64**(10), e202421101 (2025). https://doi.org/10.1002/anie.202421101
100. M.S. Kim, Z. Zhang, P.E. Rudnicki, Z. Yu, J. Wang et al., Suspension electrolyte with modified Li^+ solvation environment for lithium metal batteries. Nat. Mater. **21**(4), 445–454 (2022). https://doi.org/10.1038/s41563-021-01172-3
101. R. Xu, X.-Q. Zhang, X.-B. Cheng, H.-J. Peng, C.-Z. Zhao et al., Artificial soft–rigid protective layer for dendrite-free lithium metal anode. Adv. Funct. Mater. **28**(8), 1705838 (2018). https://doi.org/10.1002/adfm.201705838
102. S. Ni, M. Zhang, C. Li, R. Gao, J. Sheng et al., A 3D framework with $Li_3N–Li_2S$ solid electrolyte interphase and fast ion transfer channels for a stabilized lithium-metal anode. Adv. Mater. **35**(8), 2209028 (2023). https://doi.org/10.1002/adma.202209028